

Bathymetric prediction from dense satellite altimetry and sparse shipboard bathymetry

Walter H. F. Smith

NOAA Geosciences Lab, National Ocean Service, Silver Spring, Maryland

David T. Sandwell

Scripps Institution of Oceanography, La Jolla, California

Abstract. The southern oceans (south of 30°S) are densely covered with satellite-derived gravity data (track spacing 2–4 km) and sparsely covered with shipboard depth soundings (hundreds of kilometers between tracks in some areas). Flexural isostatic compensation theory suggests that bathymetry and downward continued gravity data may show linear correlation in a band of wavelengths 15–160 km, if sediment cover is thin and seafloor relief is moderate. At shorter wavelengths, the gravity field is insensitive to seafloor topography because of upward continuation from the seafloor to the sea surface; at longer wavelengths, isostatic compensation cancels out most of the gravity field due to the seafloor topography. We combine this theory with Wiener optimization theory and empirical evidence for gravity noise-to-signal ratios to design low-pass and band-pass filters to use in predicting bathymetry from gravity. The prediction combines long wavelengths (>160 km) from low-pass-filtered soundings with an intermediate-wavelength solution obtained from multiplying downward continued, band-pass-filtered (15–160 km) gravity data by a scaling factor S . S is empirically determined from the correlation between gravity data and existing soundings in the 15–160 km band by robust regression and varies at long wavelengths. We find that areas with less than 200 m of sediment cover show correlation between gravity and bathymetry significant at the 99% level, and S may be related to the density of seafloor materials in these areas. The prediction has a horizontal resolution limit of 5–10 km in position and is within 100 m of actual soundings at 50% of grid points and within 240 m at 80% of these. In areas of very rugged topography the prediction underestimates the peak amplitudes of seafloor features. Images of the prediction reveal many tectonic features not seen on any existing bathymetric charts. Because the prediction relies on the gravity field at wavelengths <160 km, it is insensitive to errors in the navigation of sounding lines but also cannot completely reproduce them. Therefore it may be used to locate tectonic features but should not be used to assess hazards to navigation. The prediction is available from the National Geophysical Data Center in both digital and printed form.

Introduction

Topographic elevations are a fundamental physical characteristic of a planet, and yet the topographies of Mars [Carr *et al.*, 1977] and Venus [Ford and Pettengill, 1992] are better mapped than that of most oceanic areas of Earth [Smith, 1993]. In the Southern Ocean there are many gaps of hundreds of kilometers between available bathymetric survey tracks (Figure 1), and many of the data are of poor quality. In some areas, the majority of available data were collected with only celestial navigation and discrepancies in depths reported at intersecting survey tracks exceed 100–250 m at half of the track crossings [Smith, 1993]. The area south of 30°S has the least detailed bathymetric coverage but the most detailed gravity coverage thanks to recent declassification of Geosat Geodetic Mission (GM) altimeter data [Marks *et al.*, 1993]. Figure 2 shows the ground tracks of the Seasat, Geosat, and ERS 1 satellites used by Sandwell and Smith [1992] to compile

a marine gravity field (top), and the tracks of available shipboard depth soundings [Smith, 1993; National Geophysical Data Center, 1993] (middle). Also shown (bottom) are local plate boundaries and a port (Easter Island); the ship coverage is biased toward ports and tectonic features, while the satellite coverage is uniform.

Marine gravity anomalies and seafloor topography can be highly correlated over a band of wavelengths [McNutt, 1979; Smith and Sandwell, 1992; Neumann *et al.*, 1993] so that ocean depths may be inferred from sea surface gravimetry. This was first suggested in the 19th century by Siemens [1876], but it was more than a century later when Dixon *et al.* [1983] demonstrated that the technique was feasible. Dixon *et al.* used profiles of geoid height data obtained along tracks of the Seasat satellite altimeter in an area where the bathymetry was already well known from conventional surveys. This "ground truth" allowed Dixon *et al.* to demonstrate that the predictions depended strongly (± 1 km of topography) on the assumed form of isostatic compensation, and that topographic features out of the profile plane also had a strong influence on the solution. Subsequent studies [White *et al.*, 1983; Baudry *et al.*, 1987; Craig and Sandwell, 1988; Jung and Vogt, 1992;

Goodwillie and Watts, 1993] have also been confined to the vertical plane under altimeter profiles and have thus been forced to make some assumptions about symmetry because of their lack of gravity data in the across-track direction. Now that complete gravity coverage in two horizontal dimensions is available from the Geosat GM data, it is time to attempt bathymetric prediction throughout the southern oceans.

In this paper, we present a new technique which makes full use of the Geosat GM data, avoids most assumptions about isostatic compensation, and allows for regional variations in the correlation between bathymetry and gravity. We show that these regional changes are necessary to accommodate changes in the thickness of sediments on the ocean floor. The images of the seafloor we obtain resolve tectonic details to 5–10 km in location and within 100–250 m in depth in many cases. However, the method underestimates peak amplitudes in rugged areas and at very tall seamounts, so it is not suitable for charting hazards to navigation. In the next section we give a broad overview of the technique; later sections will explain each step more fully.

General Description

The relationship between seafloor topography and sea surface gravity is conveniently described by functions which depend on the wavelength of the topography [Dorman and Lewis, 1970; McKenzie and Bowin, 1976]. Theoretical and empirical studies (discussed below) suggest that we can hope for correlation between gravity and bathymetry only in a limited band of wavelengths between about 15 and 160 km. The shorter-wavelength part of the gravity field (<15 km) is attenuated by upward continuation from the seafloor to the sea surface so the signal-to-noise ratio is small, and it is unsafe to attempt prediction. Similarly, at longer wavelengths (>160 km), seafloor topography can be isostatically compensated so that it produces little or no gravity anomaly. Our approach is to use gravity to predict bathymetry in the 15–160 km band. Shorter-wavelength topography (<15 km) can only be recovered through detailed shipboard surveys, while longer-wavelength (> 160 km) topography may be constrained by low-pass-filtering grids of existing ship soundings.

Within the prediction band, the ratio of topography to gravity, $S(x)$, is determined empirically in areas where these are well correlated. The topography-to-gravity ratio is allowed to vary at long wavelengths (> 160 km) to accommodate regional variations in sediment thickness and seafloor density. High topography-to-gravity correlations are generally found over unsedimented topography because of the large seawater-to-rock density contrast. Low correlations are generally found in areas where the topography is buried by thick sediments; in these areas the buried structures produce gravity anomalies, while the seafloor relief is low. Fortunately, these sedimented areas are nearly flat at short wavelengths so that we may take $S=0$ here. In practice, we band-pass filter the gridded ship soundings and gravity and downward continue the gravity to the regional seafloor depth. The theory predicts a linear relationship between these data, and so we use a linear regression method to estimate both topography-to-gravity ratio and correlation. This method, which we call the "inverse Nettleton procedure," uses only those points in the grid where actual soundings are available. The total predicted bathymetry $b_p(x)$ is the sum of the passband prediction and long-wavelength regional depth $d(x)$:

$$b_p(x) = d(x) + S(x)g(x), \quad (1)$$

where the passband prediction is the product of the band-pass-filtered and downward continued gravity $g(x)$ and the scaling factor $S(x)$. Note that with this method, $b_p(x)$ will not fit the original soundings exactly. Soundings which are misplaced by a few tens of kilometers will introduce little error into $d(x)$ but would have a severe effect at shorter wavelengths, where we choose to rely on the gravity data to locate the predicted features.

An example is shown in Plate 1. The top image shows the sea level gravity field of Sandwell and Smith [1992], while the middle image shows the predicted bathymetry. For comparison, the bottom image shows the best available gridded bathymetry data known as ETOPO-5 [National Geophysical Data Center, 1988], which is based on the earlier DBDB-5, or SYNAPS data [Van Wyckhouse, 1973] (ETOPO-5, Earth TOPOgraphy-5 minute; DBDB-5, Digital Bathymetric Data Base-5 minute; SYNAPS, SYNthetic BATHymetric Profiling System). The prediction shares some features with each of these other images, and one could imagine combining the regional features of ETOPO-5 with the local features of the gravity to produce the predicted bathymetry. If $S(x)$ were everywhere constant and ETOPO-5 matched $d(x)$ exactly at long wavelengths, then the middle image (the prediction) would be a simple combination of the top and bottom images. In fact, ETOPO-5 does not fit the ship data very well [Smith and Wessel, 1990; Smith, 1993], and variations in $S(x)$ make the prediction more complicated, and more interesting. We find that S varies geographically in accordance with the thickness of sediment cover, and in some areas, gravity and topography are uncorrelated and $S = 0$. Estimation of S at the areas labeled A, B, and C in Plate 1 will be discussed in the section on the inverse Nettleton procedure.

Data Preparation

Digital shipboard soundings south of 30°S were derived from two sources. The primary source was assembled from the Lamont-Doherty Earth Observatory holdings and put through extensive quality control procedures [Smith, 1993]. This was augmented by data compiled by the National Geophysical Data Center [1993]. Most of these additional data were recent surveys along the Antarctic coast by foreign Antarctic agencies, particularly the British and Japanese; a few were newly contributed data from domestic laboratories. Notable among these were a R/V *Moana Wave* survey of the Australian-Antarctic Discordance and R/V *Thomas Washington* surveys of the East Pacific Rise and the Louisville Ridge. All new data from the CD-ROM were put through the quality screening recommended by Smith [1993]. The Japanese data were found to have navigation reporting errors when latitude or longitude was equal to an integer number of degrees; these erroneous data were deleted. A total of 581 legs were used in our study (Figure 1).

These data were gridded onto a mesh having 20 samples per degree longitude and 40 samples per degree latitude and spanning an area between 25.8°S and 73.8°S. This procedure allowed us to use results in the area 30°–70°S without edge effects from our filters and resulted in grid "cells" which are squares approximately 2.75 km on a side at 60°S. The grid was prepared by first assigning all soundings to their nearest grid point and then at each grid point with one or more soundings

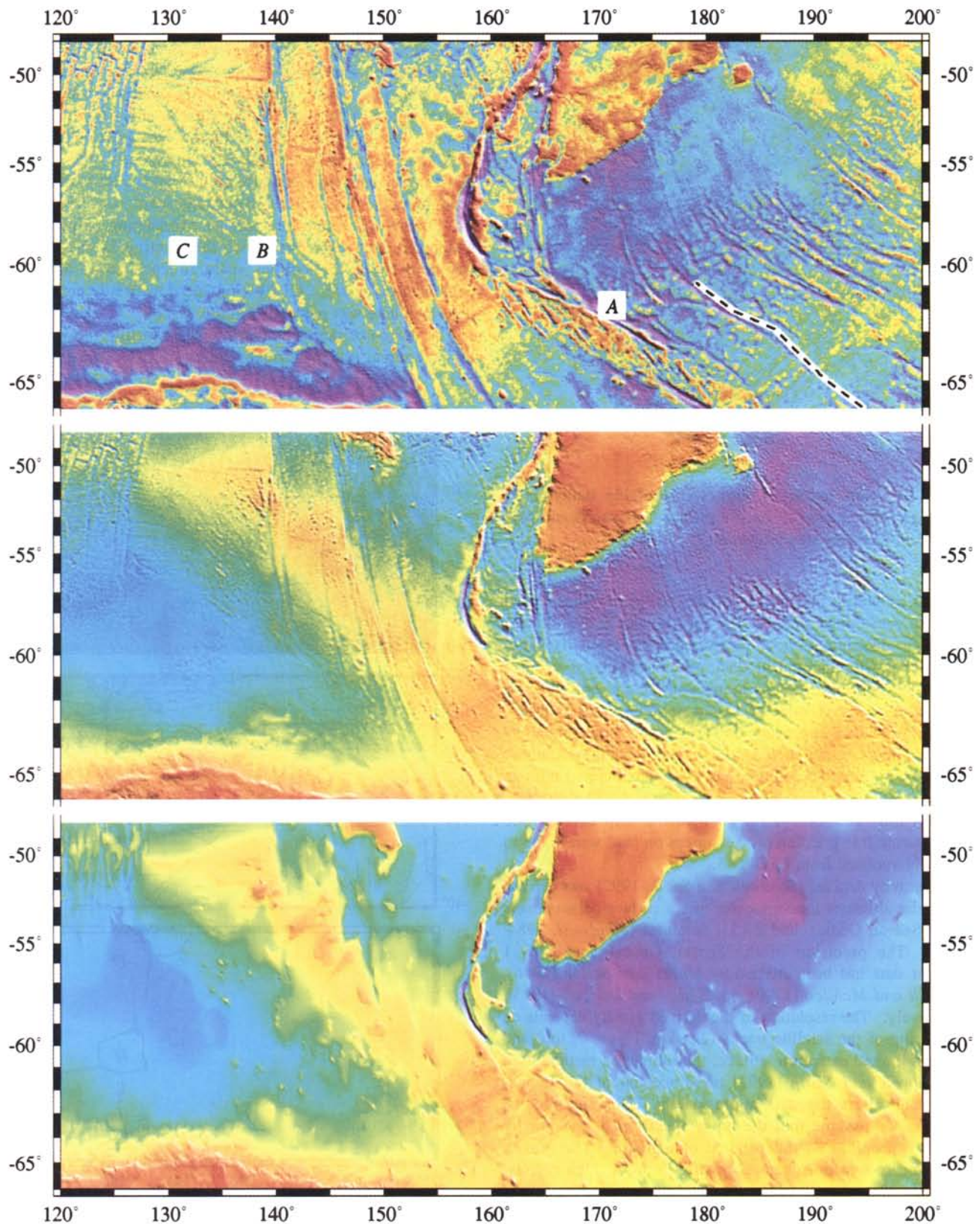


Plate 1. (top) Free-air gravity field from *Sandwell and Smith* [1992]. Areas labeled A, B, and C are discussed in connection with Figure 6, and the dashed line is the location of the profile shown in Figure 8. (middle) Bathymetric prediction made from gravity by the method of this paper. (bottom) ETOPO-5 bathymetry for comparison.

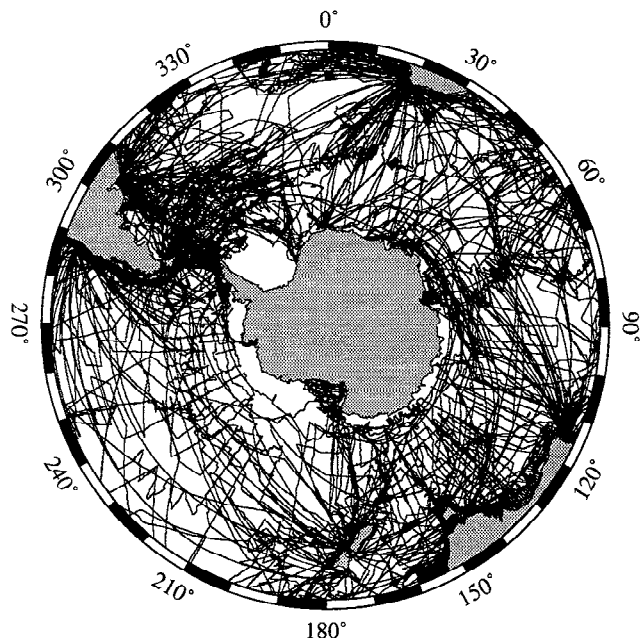


Figure 1. Ship tracks of digitally available bathymetric soundings. One-quarter of Earth's surface is shown (south pole to 30°S) in an equal-area projection.

assigned, retaining the median of the assigned values. Grid points so constrained were marked for use later in the "inverse Nettleton" determination of the topography-to-gravity ratio. Grid points without control data were interpolated using a continuous curvature spline in tension [Smith and Wessel, 1990] with a tension value of 1, corresponding to a harmonic spline. With this approach, the grid points constrained by ship soundings retain their initial values, and the harmonic spline assures that the solution has local maxima and minima only at these points [Smith and Wessel, 1990]. The resulting grid has hills and valleys only where the ship data require them. During this gridding process, areas on land were fixed to values interpolated from ETOPO-5.

The gravity data set [Sandwell and Smith, 1992] was derived from radar altimeter measurements of sea surface heights made by the Seasat, Geosat, and ERS 1 satellites [Sandwell, 1984, 1992]. The precision of the Seasat, Geosat, and ERS 1 altimeter data has been studied by Marks and Sailor [1986], Sandwell and McAdoo [1990], and Sailor and Driscoll [1993], respectively. The resolution of the derived gravity depends on the spacing of the satellite tracks (2–4 km, Figure 2, top) and also to a limited extent on latitude; the estimation method used by Sandwell and Smith [1992] takes account of this dependence and filters the data appropriately. Therefore in the appendix we assume that the noise spectrum of the gravity map is isotropic, i.e., independent of azimuth. The gravity grid has a root-mean-square error of 3–5 mGal, high correlation with ship gravity measurements at wavelengths longer than 20 km [Smith et al., 1993], and high correlation with ship bathymetry for wavelengths greater than 26 km [Neumann et al., 1993]. The gravity grid was resampled onto the same grid as the initial bathymetry grid.

Admittance Theory

Flexural isostatic compensation theory is used as a guide to design various low-pass, high-pass, and band-pass filters used

in the bathymetric prediction procedure outlined above. Here we give a detailed description of the filter design and implementation. The theory is developed in terms of the Fourier transforms of gravity and topography data. A flat Earth approximation is used throughout the analysis because the longest cutoff wavelength in any filter is only 160 km, which is much less than the radius of Earth. Our grids are sampled with equal spacing in latitude and longitude, so the distance between adjacent east-west grid points varies with latitude. To accommodate this latitude-dependent scale, we divided the 30°–70° latitude range into smaller overlapping strips, cosine windowed each strip, performed the filtering by fast Fourier transform with the correct scale in each strip, and then combined the strips. All filtering and downward continuation described here was performed in this fashion.

The design of the bathymetric prediction filter is motivated by theoretical and empirical studies of $Z(k)$, known as the

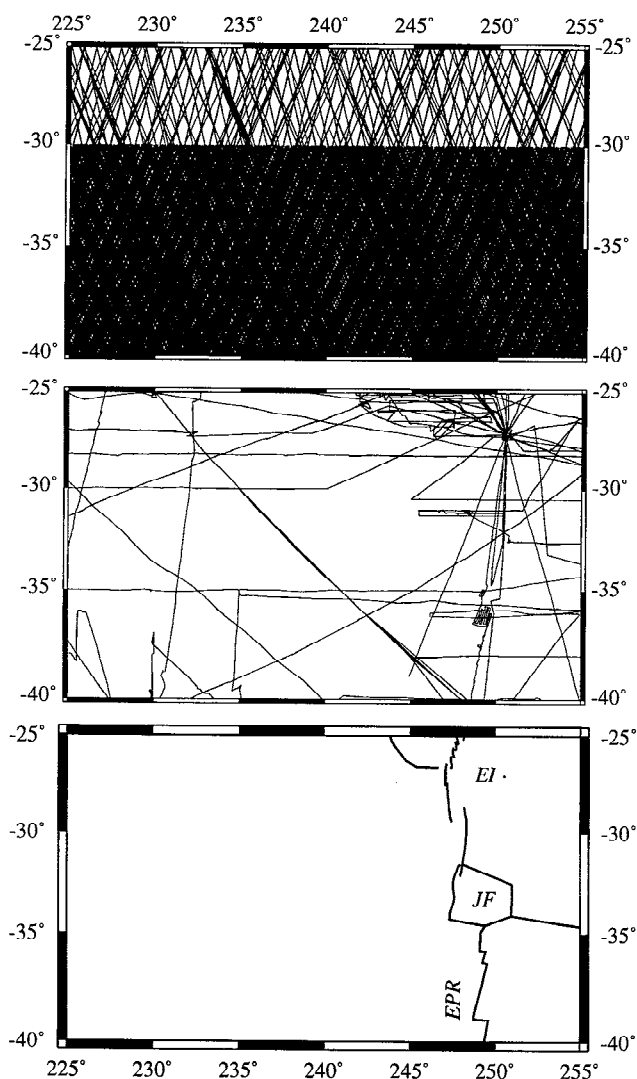


Figure 2. Mercator track maps for an area of the South Pacific 2790 km E-W by 1670 km N-S. (top) Seasat, ERS 1, and Geosat satellite tracks. Geosat GM data available south of 30°S are spaced 2–4 km apart; north of 30°S there are 40 by 100 km gaps in coverage. (middle) Ship sounding lines in same area. There are 500 by 750 km gaps, and coverage is biased toward ports (Easter Island) and particular features (East Pacific Rise). (bottom) Geographic references. EI, Easter Island; EPR, East Pacific Rise; JF, Juan Fernandez microplate.

gravitational "admittance" in the literature [Lewis and Dorman 1970; Dorman and Lewis, 1970; McKenzie and Bowin, 1976; Watts, 1978, 1979; McNutt, 1979]. $Z(k)$ is the transfer function of a linear, isotropic, and spatially invariant filter which takes a topography field $h(\mathbf{x})$ as input and produces a gravity field $g(\mathbf{x})$ as output. In the Fourier transform domain this is written

$$G(\mathbf{k}) = H(\mathbf{k})Z(k). \quad (2)$$

The definitions of Bracewell [1978] are used here for two-dimensional Fourier and Hankel transforms: $H(\mathbf{k})$ is the Fourier transform of $h(\mathbf{x})$, where $\mathbf{x} = [x, y]$ and $\mathbf{k} = [u=1/\lambda_x, v=1/\lambda_y]$. A one-dimensional Hankel transform is used for isotropic functions dependent only on the scalar distance $r = |\mathbf{x}|$, and scalar wavenumber $k = |\mathbf{k}|$; $Z(k)$ is the Hankel transform of $z(r)$. In formulating (2), the topography $h(\mathbf{x})$ is defined as the local relief of the seafloor measured from a constant regional depth d . Parker [1973] has shown that (2) is only approximately true, as the correct relationship is nonlinear. The approximation is a good one when h is small compared with d . We retain this linear approximation throughout the paper and discuss its limitations in evaluating the bathymetric prediction.

In flexural isostatic compensation theory, the seafloor topography h acts as a load on a thin elastic lithosphere, and the lithosphere flexes under the load in a linear, spatially invariant, and isotropic manner. The gravity field $g(\mathbf{x})$ is the sum of the direct topographic effect and its isostatic compensation. When the wavelength of the topographic load is much less than the flexural wavelength of the lithosphere (defined below), the admittance function is given by the uncompensated model

$$Z(k) = 2\pi\Gamma\rho \exp[-2\pi kd], \quad (3)$$

where d is the regional depth, ρ is the density of the seafloor relative to seawater, and Γ is the Newtonian gravitational constant ($2\pi\Gamma\rho$ is known as the Bouguer constant). The exponential decay with increasing wavenumber is known as "upward continuation" and is shown in Figure 3 (solid curve). The gravity anomaly produced by an uncompensated conical seamount (2 km high and 60 km in diameter) is shown in Figure 4 (long dashed curve). The exponential decay in Z acts as a smoothing filter, so that the sharp edges in the topography are not present in the gravity profile. Also, the peak amplitude of the gravity anomaly is less than $2\pi\Gamma\rho$ times the peak amplitude of the topography. Implicit in the bathymetric prediction problem is the need to undo this smoothing, which is unstable.

When the wavelength of the topographic load matches or exceeds the flexural wavelength, the plate deflects under the load causing a downwarping of the Mohorovicic discontinuity (Moho), $m(\mathbf{x})$. Assuming that the deflection of the plate is much less than the flexural wavelength and the plate has no inelastic response, the Moho deflection is related to the topographic load by another linear isotropic filter [Banks *et al.*, 1977]:

$$M(\mathbf{k}) = -\frac{(\rho_c - \rho_w)}{(\rho_m - \rho_c)} H(\mathbf{k})\Phi(k), \quad (4)$$

with

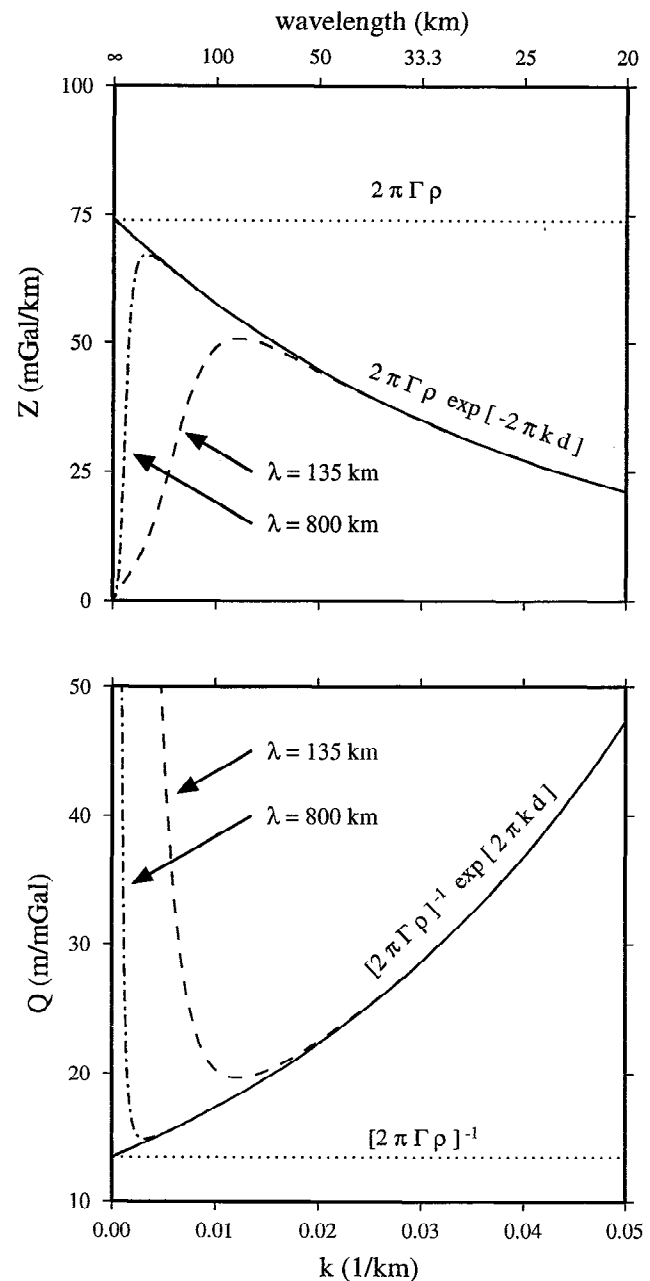


Figure 3. Transfer functions versus wavenumber. Scale at bottom in wavenumber; scale at top in equivalent wavelength. (top) Z , the transfer function for topography input and gravity output. A constant value (dotted line) holds for uncompensated topography on the gravity observation level. Upward continuation to a level d produces exponential decay (solid curve). Isostatic compensation causes Z to approach zero at wavelengths longer than a parameter λ (dashed and dot-dashed curves). (bottom) $Q = Z^{-1}$, the transfer function for gravity input and topography output. Each curve is the reciprocal of the corresponding one in the top panel.

$$\Phi(k) = [1 + (\lambda k)^4]^{-1}. \quad (5)$$

Here $(\rho_c - \rho_w)$ is the density contrast of the seafloor relative to seawater and $(\rho_m - \rho_c)$ is the density contrast of the mantle relative to the crust. The flexural wavelength λ is the wavelength at which $\Phi = 0.5$; at wavelengths much longer than λ the topography is Airy compensated, while at wavelengths

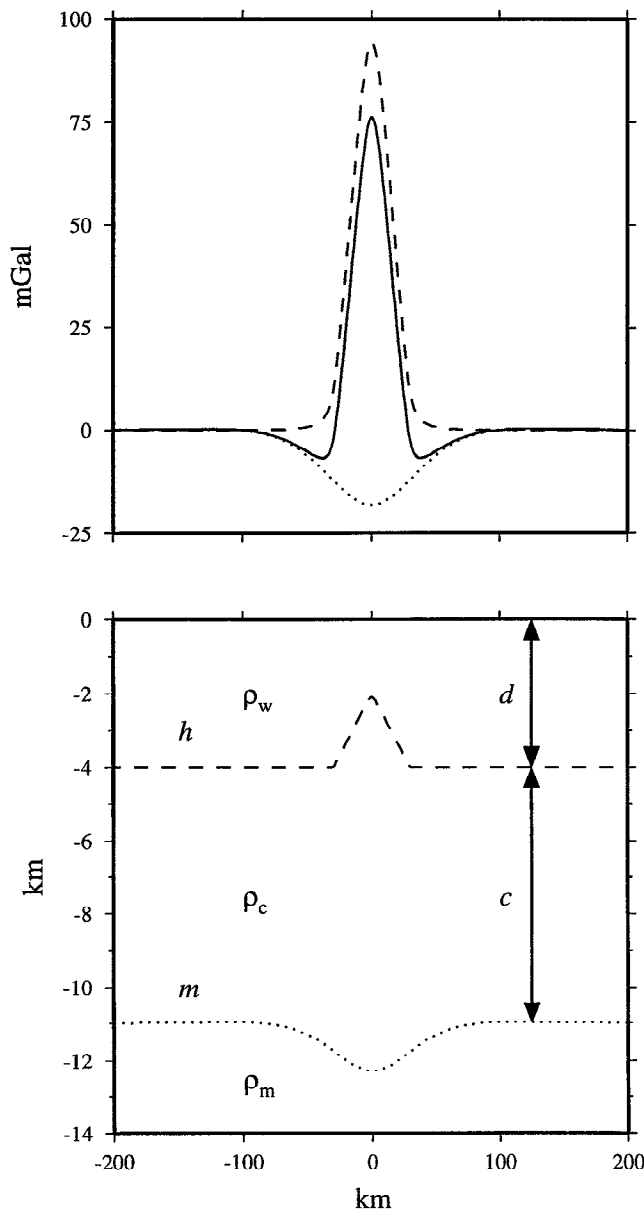


Figure 4. (top) Gravity anomalies due to a seamount. Dashed curve, effect of topography only; dotted curve, effect of compensation only; solid curve, combined effect. (bottom) Cross section through the ocean crust showing a conical seamount (h , dashed curve) and the moho deflection (m , dotted curve) which compensates it. Also shown are water depth d , crustal thickness c , and densities ρ_w , ρ_c , ρ_m appearing in the text.

much shorter than λ the topography is uncompensated. The admittance function for this model is

$$Z(k) = 2\pi\Gamma\rho \exp[-2\pi kd] \{ 1 - \exp[-2\pi kc] \Phi(k) \} \quad (6)$$

where c is the normal crustal thickness (7 km) and $\rho = \rho_c - \rho_w$. Admittance functions for λ of 800 km and 135 km are shown in Figure 3 (dashed/dotted curves); these are typical minimum and maximum values for λ . The isostatic compensation of the conical seamount is diagrammed in Figure 4 (bottom) for $\lambda = 135$ km. The gravity effect of the Moho deflection is shown

by the dotted curve in the top panel of Figure 4, and the combined gravity is shown as the solid curve. The filter (6) reduces the peak gravity amplitude relative to the uncompensated model and introduces negative side lobes so the resulting gravity does not look exactly like the topography. Attempts to recreate the missing signal with an inverse filter are unstable.

Window Carpentry and Filtering

By analogy with (2), we may define a linear, isotropic, spatially invariant process which takes gravity as input and produces seafloor topography as output; it will have a transfer function $Q(k)$ such that

$$H(k) = G(k)Q(k). \quad (7)$$

Inspection of equations (2) and (7) suggests that $Q(k) = Z^{-1}(k)$ [Dixon *et al.*, 1983]. However, this definition results in a function which approaches infinity at both the low and high wavenumber ends of the spectrum (Figure 3, bottom) and whose Hankel transform does not exist. Thus topography prediction using (7) is unstable. At short and long wavelengths any noise in the gravity field, or slight deviations in density from the assumed density, will be greatly amplified resulting in a poor prediction. Moreover at long wavelengths, uncertainty in the flexural wavelength will result in a poor prediction because Q is very sensitive to λ . Thus Q must be taken as a band-limited approximation of Z^{-1} [Dixon *et al.*, 1983]

$$Q(k) = Z^{-1}(k)W(k), \quad (8)$$

where $W(k)$ is any band-pass filter (also called a spectral window function) which stabilizes the prediction problem and forces $Q(k)$ to have a Hankel transform which exists. This means that predictions formed using equation (7) can only resolve a limited range of wavelengths in h .

Dixon *et al.* [1983] used the above isostatic flexure theory for Q to attempt a prediction. Their study covered a limited area so they were able to assume that d and ρ were constants, as the above theory requires. They chose a rectangular window $W(k)$, which produced spurious oscillations in their predicted bathymetry due to Gibbs' phenomenon [e.g., Bracewell, 1978]. Their window included some isostatically compensated wavelengths in the passband, and so they found that their results depended strongly on the value of λ they assumed: predicted heights of seamounts varied by 1 km according to the choice of λ . Finally, and perhaps most importantly, they used only one-dimensional profiles of gravity data and assumed that both the gravity and topography fields were lineated perpendicular to the track, when in fact their study area (the Musician Seamounts) contains many pointlike features.

The flexural wavelength of the lithosphere, λ , is related to the thickness of the elastic part of lithosphere which in turn increases with the age of the lithosphere [Watts, 1978; Caldwell and Turcotte, 1979; Sandwell and Schubert, 1982] because the base of the elastic layer follows an isotherm. The thinnest lithosphere is found at the seafloor spreading ridges. Over the fast spreading East Pacific Rise, elastic thicknesses range between 2 and 6 km, while over the slower spreading Mid-Atlantic Ridge, the elastic plate is a somewhat thicker 7–

13 km [Cochran, 1979]. All of the ridges south of 30°S are spreading at rates of 98 mm/yr or less. We follow Watts *et al.* [1980] and assume an elastic thickness of 5 km ($\lambda = 135$ km) as a minimum value. Topographic features on the seafloor which form away from the ridge axis may exhibit admittance functions indicating a range of elastic thicknesses [Watts, 1978], and in some cases, quite different values may be found within 150 km of one another [Smith *et al.*, 1989]. If the cooling of the lithosphere follows the plate model of Parsons and Sclater [1977], then the maximum value of λ we would expect to find is about 800 km; this range of wavelengths between approximately 135 and 800 km has been called the "diagnostic waveband of flexural response" [Watts, 1983].

We designed our filter $W(k)$ as the product of two filters $W_1(k)$ and $W_2(k)$ to suppress the long- and short-wavelength singularities, respectively. To design W_1 , we assumed that $\lambda \geq 135$ km in the southern oceans, and we formed the function Q_∞/Q_{135} , where the subscript indicates the λ value and $\lambda = \infty$ corresponds to the uncompensated case (solid curve in Figure 3, bottom); this ratio removes the effects of d and ρ and isolates the effect of λ . From equation (6) it follows that

$$\frac{Q_\infty}{Q_{135}} = 1 - \exp[-2\pi kc] \Phi_{135}(k), \quad (9)$$

where c is the thickness of the crust. The ratio Q_∞/Q_{135} is well approximated by a simpler Gaussian high-pass filter with parameter $s = 30$ km

$$W_1(k) = 1 - \exp[-2(\pi ks)^2]. \quad (10)$$

$W_1 = 0.5$ when $k^{-1} = 160$ km. This filter removes the flexural waveband and longer wavelengths and is easier to compute in the form (10) than (9).

The low-pass filter W_2 was designed to suppress the high wavenumber band where the exponential growth in Q due to the downward continuation becomes large. At wavelengths where the gravity data are very accurate, W_2 should be near 1 (the passband), while at wavelengths where the gravity data are unreliable, W_2 should be near 0 (the stopband). The choice of transition wavelength is important; if it is too low, the predicted topography will have low resolution, while if it is too high, the prediction will be overwhelmed by noise. If the noise-to-signal ratio as a function of wavenumber $R(k)$ is known, then W_2 can be designed so as to minimize the mean square error in the downward continued gravity field (and hence the predicted topography). This method of optimizing filters to minimize the variance in an estimated signal is from Wiener [1949]. In the appendix we sketch the derivation of the Wiener filter and show how published studies of the spectral coherency in Geosat altimeter data [Sandwell and McAdoo, 1990] can be used to make an inspired guess at the functional form of $R(k)$. It turns out that W_2 depends on the regional water depth d , because the gravity signal strength decays at a rate depending on d (Figure 3, top) while the noise process is independent of d . The form we adopted for W_2 is

$$W_2(k) = \{1 + Ak^4 \exp[4\pi kd]\}^{-1} \quad (11)$$

which can be found by substituting equation (A13) into (A8). In (11), A is a constant chosen so that $R(k)$ fits the observed spectral coherency; we used $A = 9500 \text{ km}^4$. With this value,

$W_2 = 0.5$ when $k^{-1} = 15, 20$, and 25 km, for water depths of 2, 4, and 6 km, respectively.

The combined filter $W(k) = W_1(k)W_2(k)$ is shown in Figure 5 (top), and its Hankel transform $w(r)$ in Figure 5 (bottom). The dotted, solid, and dashed curves correspond to water depths of 2, 4, and 6 km, respectively. The impulse response $w(r)$

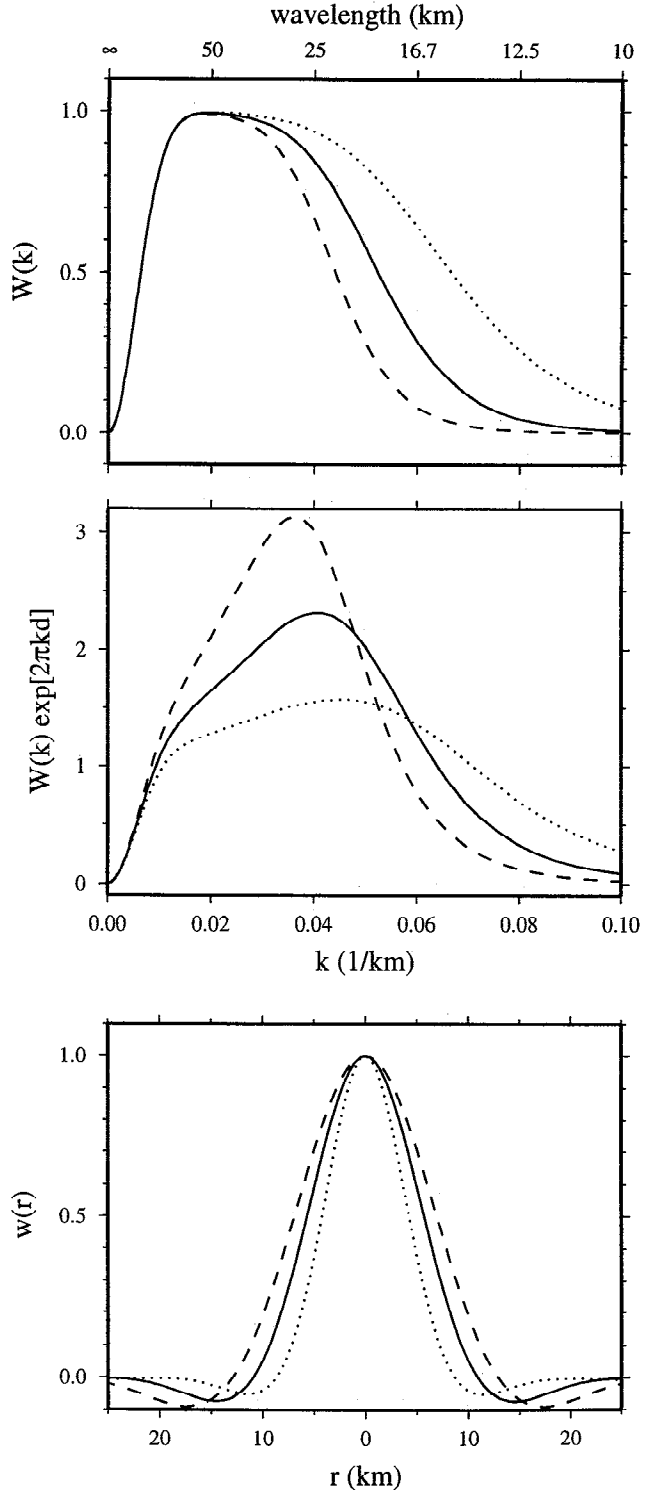


Figure 5. The filters (top) $W(k)$ and (middle) $W(k) \exp[2\pi kd]$, and (bottom) the impulse response $w(r)$. Dotted, solid, and dashed curves correspond to water depths of 2, 4, and 6 km, respectively.

shows that the filter acts as a local averaging operation, which limits the resolution of our prediction. One definition of resolving power [Backus and Gilbert, 1968] concerns the averaging length of a linear system, which Constable and Parker [1991] take as the width of the impulse response at half-maximum amplitude. For $d = 2, 4$, and 6 km this width is 8.5, 11.4, and 13.8 km. Another measure of resolving power is Rayleigh's criterion as used in optical imaging systems [Goodman, 1968]; by this criterion, two point features can be distinguished if they are separated by a distance greater than the distance from the center of $w(r)$ to the first minimum. For $d = 2, 4$, and 6 km this distance is 11.2, 14.6, and 19.2 km. Because $w(r)$ depends on the water depth, our method will have higher resolution in shallow water.

The theory for $Z(k)$ and $Q(k)$ is derived assuming a constant water depth d . We allow a slowly varying water depth $d(\mathbf{x})$ by using the low-pass filtered version of the observed bathymetry grid $b_o(\mathbf{x})$:

$$D(\mathbf{k}) = B_o(\mathbf{k})[1 - W_1(k)]. \quad (12)$$

The local seafloor topography is the band-pass-filtered version of the observed bathymetric grid:

$$H(\mathbf{k}) = B_o(\mathbf{k})W(k), \quad (13)$$

where d is set to 0 in (11) as used in (13).

Finally, the downward continued and band-pass-filtered gravity $g(\mathbf{x})$ is related to the observed gravity $g_o(\mathbf{x})$ by

$$G(\mathbf{k}) = G_o(\mathbf{k})W(k)\exp[2\pi k d]. \quad (14)$$

This filter is shown in the middle panel of Figure 5. Since the depth varies spatially and (14) depends strongly on depth, a different filter was applied to each grid cell. In practice, an initial solution was calculated using (14) for constant values of d , in multiples of 1 km of depth. Then the actual $g(\mathbf{x})$ was obtained at each grid cell \mathbf{x} using $d(\mathbf{x})$ and linearly interpolating among the solutions found using constant d . In this manner, $g(\mathbf{x})$ is the band-passed gravity field "draped over" the regional depth $d(\mathbf{x})$. We are now assuming that the theory derived using a constant d can be applied locally (at wavelengths shorter than 160 km) since $d(\mathbf{x})$ varies only regionally (at wavelengths longer than 160 km).

Inverse Nettleton Procedure

After the above processing, we have all but one of the components needed for the bathymetric prediction given by equation (1). The total predicted bathymetry $b_p(\mathbf{x})$ is the sum of the passband prediction $S(\mathbf{x})g(\mathbf{x})$ and long-wavelength regional depth $d(\mathbf{x})$. Since the analysis is limited to the uncompensated band, the theoretical value of S is $[2\pi\Gamma\rho]^{-1}$, where ρ is the density of the seafloor material relative to seawater. If g and h obey the theory, then $h = Sg$. Our task is to determine whether g and h are in fact correlated and the best value of S to predict h from g . Nettleton [1939] suggested that the appropriate density for Bouguer gravity reductions could be found by trial and error, selecting the density which yielded the Bouguer correction looking most like the free-air anomaly. In essence, Nettleton's method for density estimation is a regression procedure: find ρ such that $2\pi\Gamma\rho h$ best fits g by regression of g onto $2\pi\Gamma\rho h$. Our problem is the

inverse of Nettleton's (hence "inverse Nettleton procedure"), but we use a robust regression technique constrained to pass through the origin.

In order to obtain $S(\mathbf{x})$ as a smoothly varying function with spectral content comparable to $d(\mathbf{x})$, we estimate S at points on a grid (the "Nettleton grid") sampled 2.5 degrees in longitude and 1.25 degrees in latitude. This yields a grid spacing of 135 km at 60°S. At each Nettleton grid point we form the set of all g, h pairs which are at points in the h grid originally constrained by ship soundings and which are within a 135 km radius of the Nettleton grid point. Each pair is assigned a weight based on its distance from the estimation point using a cosine window. If there are n data in the set then the sum of the weights will be about $0.3n$ when the data are distributed uniformly through the region $r < 135$ km. We found that weight sums of 10 or more gave good estimates of S .

In Plate 1, three areas are labeled A, B, and C, and the data from these areas used in the inverse Nettleton procedure are shown in Figures 6a, 6b, and 6c, respectively. Area A is located on young seafloor along the Pacific-Antarctic Ridge, area B is on older seafloor in the vicinity of a large fracture zone system, and area C is on the South Indian Abyssal Plain. Sediment cover is negligible in area A and increases from A to B to C, reducing the spread in the distributions of g and h . Figures 6a, 6b, and 6c show histograms of g in the top panel, h in the second panel, and the scatter plot of h versus g in the bottom panel. The scatter plots are shown at the same scale in each figure to illustrate the reduction in spread caused by the sediment cover. The histograms change bin width and scale from one figure to the next in order to show the data distributions. The effect of increasing sediment cover is to increase the skewness of the distributions, particularly in the h data.

In simple linear regression we would fit a line to g, h pairs by ordinary least squares assuming that g was known perfectly and h contained some random error. We could take S as the slope of that line. If there are errors in both g and h , simple linear regression leads to biased estimates for the slope of the regression line [Brownlee, 1965]; in this case a better estimate is $S = \pm\sigma_h/\sigma_g$, where σ_g, σ_h are the standard deviations of g and h [Bendat and Piersol, 1986]. In either case the line passes through the point with coordinates mean g , mean h , and the portion of the variance in h which can be explained by its relationship with g may be characterized by the linear correlation coefficient. The parameter estimates are maximum likelihood only if the data are drawn from a normal, or bivariate normal, distribution [Brownlee, 1965].

Because the data exhibit nonnormal distributions, we did not use the conventional standard deviation in estimating σ , the spread of the data; instead, we defined σ by $\sigma = 1.4826 \Sigma$, where Σ is the weighted median absolute value of g or h . The median absolute deviation is a well-known nonparametric estimate of the spread of a distribution, and the factor 1.4826 makes this σ equivalent to the σ of a normal distribution (the expected value for Σ of a normal distribution is $\sigma/1.4826$) [Rousseeuw and Leroy, 1987]. The weighting we applied in the calculation of Σ makes our estimate of σ depend more strongly on points near the center of the window. When the mean value of a distribution is unknown, one computes the standard deviation with respect to the mean; similarly, Σ is usually computed as the median absolute deviation of the data from some location estimate. We computed Σ using the median absolute value of the data, which is equivalent to

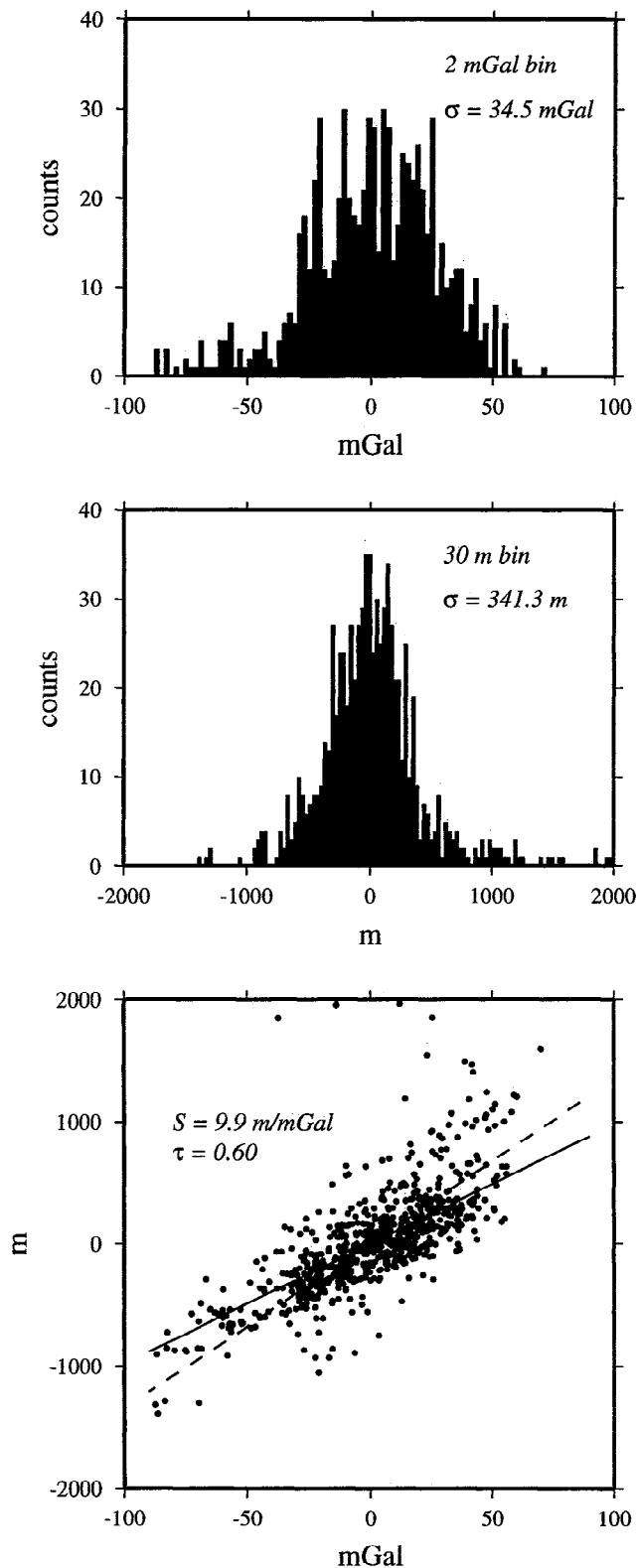


Figure 6a. Histograms and scatter plot of gravity and ship-constrained topography from area A in Plate 1, representing young seafloor with little sediment.

assuming the data are distributed around zero; this is so that if we take $S = \pm\sigma_h/\sigma_g$, then S will be the slope of a line through the origin.

We also used a nonparametric estimate of τ , the correlation between g and h , called "Kendall's tau" [Press et al., 1986].

Like the ordinary linear correlation coefficient, the magnitude of τ is ≤ 1 , with the sign indicating the sense of the correlation. The distribution of τ is known in the case of the null hypothesis (H_0) that g and h are uncorrelated, and we can calculate the confidence with which this hypothesis can be

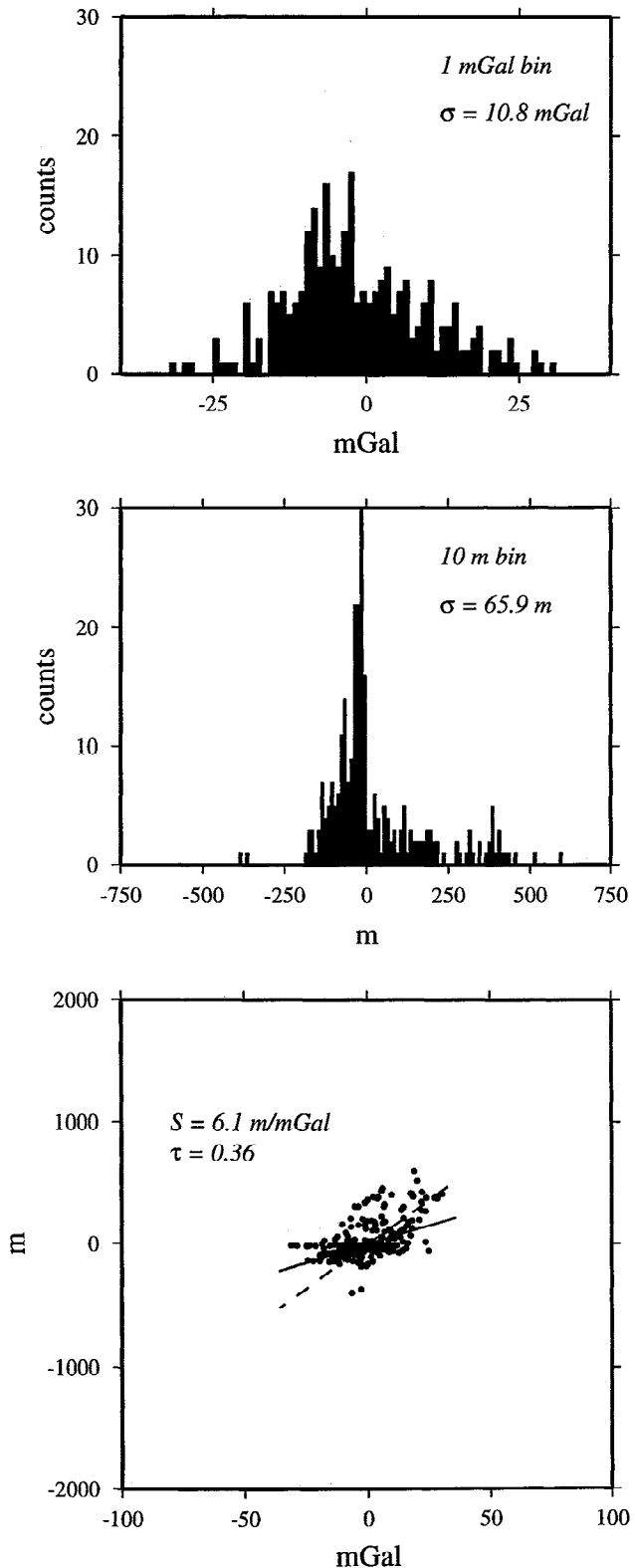


Figure 6b. Same as Figure 6a, except for area B, representing partial burial of basement by sediment.

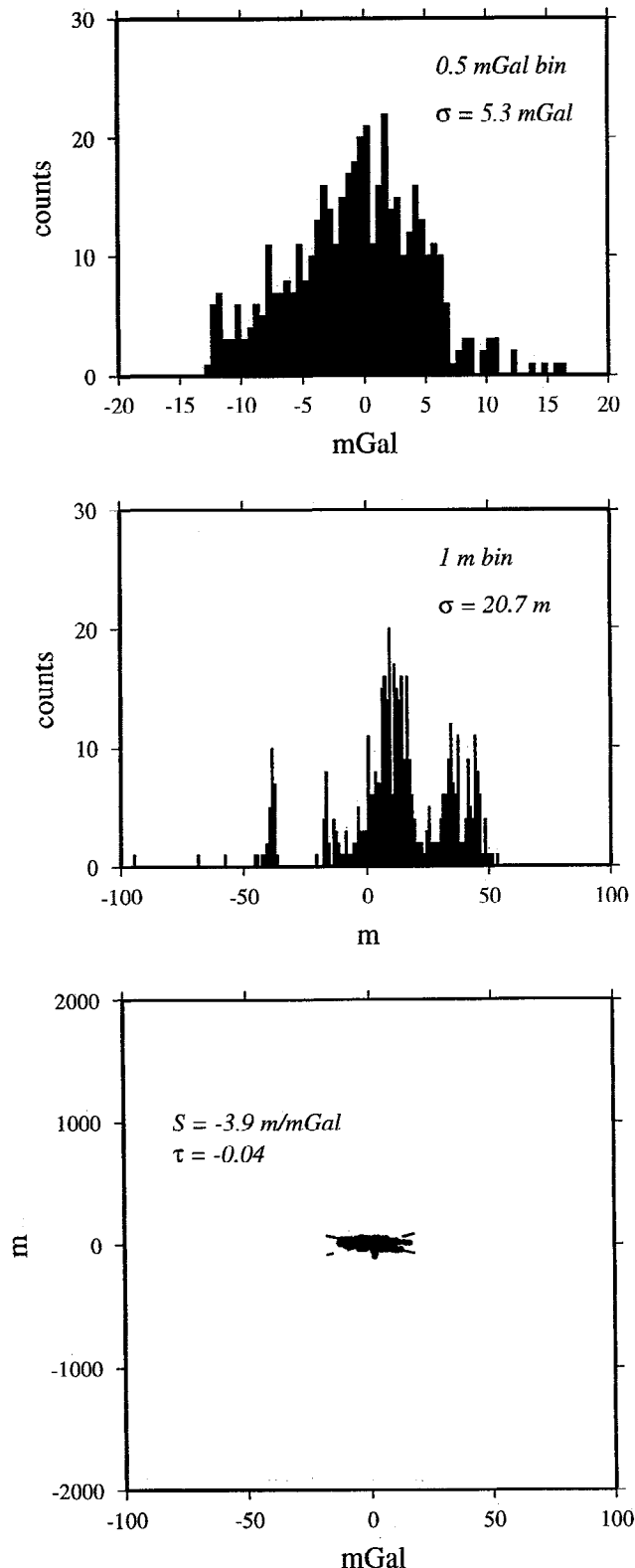


Figure 6c. Same as Figure 6a, except for area C, representing an abyssal plain.

rejected; that is, the significance of the correlation [Press *et al.*, 1986].

The scatter plots (bottom panels of Figures 6a, 6b, and 6c) show the τ value we determined for these areas. Also shown are solid and dashed lines. The solid lines are drawn through the origin with a slope given by $\pm\sigma_h/\sigma_g$, σ being estimated by the Σ method and the sign being taken from the sign of τ . The

dashed lines are formed in the same manner but using the root-weighted-mean-square to estimate σ and the ordinary linear correlation coefficient to determine the sign of the slope; these represent the weighted least squares solution. Areas A and B illustrate that the Σ method yields a line which seems to fit the majority of the data more closely; the dashed line is pulled toward the outlying data. In area C, the signs of the correlation coefficients are different, but both are so small in magnitude that the confidence that H_0 can be rejected is also small; these data show no significant correlation.

The confidence with which we can reject H_0 and the estimated value of τ for all Nettleton grid points are shown in the top two panels of Figure 7. Some of these can be related to the major geological features shown in the bottom panel of Figure 7. Both of these are shown as zero where no data are available. In most other areas, the confidence in the correlation is greater than 99%. Correlation coefficients are particularly high over some continental shelf breaks and some active plate boundaries (Mid-Atlantic and Southwest Indian Ridges; Chile, Hjort, and Tonga Trenches; Scotia Sea), as well as the aseismic Louisville and Broken Ridges. All of these are areas of large signals in g and h , similar to area A in Figure 6a. Correlations are low, and even slightly less than zero, and confidences also low, over the abyssal plains. These areas are like area C in Figure 6c. Other areas yield intermediate values. At two Nettleton grid points southwest of the intersection of the Pacific-Antarctic ridge and the Eltanin Fracture Zone system (220°E, 55°S) there is a strongly negative correlation with high confidence; this is, of course, contrary to theoretical expectations. We examined this area and found a narrow ridge in both the gravity and depth data, but in slightly different locations. The depth soundings were all collected by the R/V *Vema* using only celestial navigation, and we believe the soundings are mislocated here, causing the inverse correlation.

These experiences with estimating correlations led us to define S as follows: We only estimate S where the sum of the weights is at least 10. We take $S = \sigma_h/\sigma_g$ whenever the confidence that H_0 can be rejected is 95% or more and τ is positive. If τ is negative or the rejection confidence is less than 95%, we proceed based on the value of σ_h . If $\sigma_h < 50 \text{ m}$, we assume we have a situation like in area C, where the seafloor is nearly flat and g is uncorrelated with h ; we set $S=0$. If $\sigma_h > 50 \text{ m}$, we assume that the seafloor is rough enough that g and h would have a strong correlation if the ship data were better navigated; we leave S unspecified at this point. We feed these values of S into the Smith and Wessel [1990] gridding program used earlier for the ship data and use it to estimate $S(x)$ on the same grid mesh as the g and h grids. The result is shown in Figure 7, third panel from top. If the seafloor topography has a density of 2600–2800 kg/m^3 , appropriate for basalt, then we expect S in the range 13–16 m/mGal . Slopes in this range occur over some parts of the active ridge system. Slopes are generally less than 6 m/mGal in the abyssal plains. Intermediate values may indicate areas where large features formed at a ridge axis have been partially buried by sediment, as in area B. Much higher values are found in areas of extreme topographic variation, such as at the continental shelf breaks and the trenches.

Results

The $S(x)$ grid obtained above was combined with the downward continued, band-passed gravity $g(x)$ and low-passed

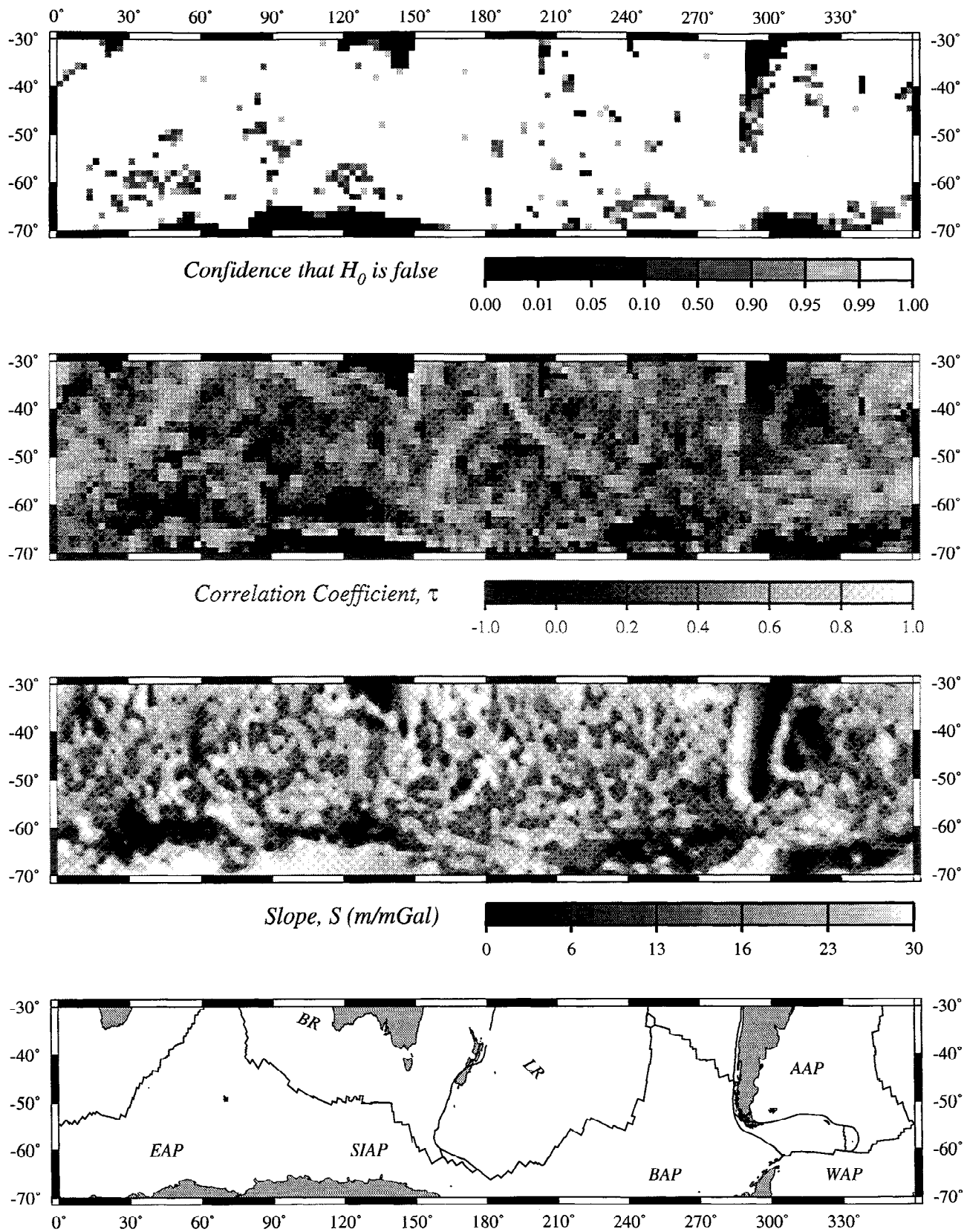


Figure 7. Results of "inverse Nettleton" procedure (top three panels), and corresponding geologic features (bottom panel). AAP, BAP, EAP, SIAP, and WAP are the Argentine, Bellingshausen, Enderby, South Indian, and Weddell Abyssal Plains. BR and LR are the Broken and Louisville Ridges. Lines indicate plate boundaries.

bathymetry $d(x)$ to form the prediction by equation (1). The results are shown as Mercator projected images in Plates 2 through 5. A large format polar stereographic projection poster is available from the National Geophysical Data Center and the digital grid file is available by anonymous ftp from Internet site ftp.ngdc.noaa.gov [Smith and Sandwell, 1994].

It is beyond the scope of this paper to present a detailed comparison between the predicted bathymetry images and previously published bathymetric maps such as the General Bathymetric Chart of the Oceans (GEBCO) [Canadian Hydrographic Service, 1981] or ETOPO-5. Moreover, there are many detailed local bathymetric maps that should be considered in such a comparison [e.g., Lonsdale, 1988; Mammerickx, 1992]. Using the digital data grid file, the reader can prepare a local map at the scale and projection needed for such quantitative comparisons. There are, however, some general features that should be noted, especially in relation to the published gravity anomaly maps.

Most short- and intermediate-wavelength features (15–160 km) apparent in the gravity map [Sandwell and Smith, 1992] are also apparent in the predicted bathymetry map. The main differences are that the bathymetric prediction contains considerable long-wavelength information and the downward continuation procedure amplifies the shortest-wavelength gravity structure with respect to the intermediate-wavelength gravity structure. The combination of these has a profound effect on the appearance of the bathymetric map. For example, the gravity anomaly map shows large-scale structures such as continental margins and oceanic plateaus as a gravity low seaward of the shelf, a gravity high inboard of the shelf and a decay of the gravity toward zero as one moves further inboard of the shelf. This is the classic gravitational edge effect of a compensated margin. When the ship soundings and gravity are processed and combined as described above, these dipolar edge effects change to the true steplike edge. There are many examples of this throughout the map; the most prominent is the Campbell Plateau (45°–55°S latitude, 165°–180° longitude; see also Plate 1). The gravity map shows gravity lows on shallow parts (< 1000 m deep) of the plateau, while the bathymetry map clearly reflects the high plateau topography.

A second major change between gravity and bathymetry occurs at isolated loads such as seamounts and plateaus containing imbedded seamounts. On the gravity map, these structures appear as an isolated gravity high ringed by a prominent gravity low. As shown in Figure 4 the gravity low reflects the component of gravity caused by downward flexure of the Moho; most seamounts do not have prominent bathymetric moats. In the above analysis we tried to avoid the longer wavelengths associated with lithospheric flexure in order to suppress these negative sidelobes. A visual examination of the bathymetric chart shows that only a few of the predicted seamounts have moats. Most show conical shapes that better reflect the true seafloor morphology. For example, predicted seamounts on the Louisville Ridge compare well with actual bathymetric profiles [Lonsdale, 1988].

There are at least two other classes of tectonic features that are enhanced and clarified by the above processing. First, while the detailed location of the spreading ridge axis is apparent in almost all locations on the gravity anomaly map, there are a couple of areas where the ridge axis location is ambiguous. For example, in the gravity map there is no clear

ridge expression of the southernmost Mid-Atlantic Ridge (45°–55°S). The bathymetric map contains longer-wavelength topographic information that creates a symmetrical crest which can be used to infer the approximate ridge axis location; morphology considerations can be used to trace the axial valley to 50°S where it ends abruptly and becomes a broad axial dome perhaps associated with the Bouvet Hot Spot. A similar situation occurs along the Southeast Indian Ridge at ~80° longitude where, using symmetry arguments, an axial valley can be located to the southeast of Amsterdam and St. Paul Islands.

Second, sharp linear structures such as transform fault valleys, transverse ridges, and fracture zones become sharper and more continuous after the above processing. For example, the long transverse ridges of the Heezen, Tharp, and Udintsev Fracture Zones (South Pacific) are readily apparent in the bathymetric chart, while they were sometimes obscured in the gravity chart by longer-wavelength information perhaps related to lithospheric flexure or thermal isostasy.

While in many cases the bathymetric map clarifies the tectonic structures, it hides many important features that are buried by sediments. Thus the gravity anomaly map may be better for investigating the tectonics of the old sedimentary basins.

Validation

In January and February of 1992, the R/V *Maurice Ewing* made a survey across the Pacific-Antarctic Rise near Fracture Zone XII (now also called the Pitman Fracture Zone) using Global Positioning System navigation and Hydrosweep multibeam sonar data. These data have not yet been released to the National Geophysical Data Center and were not available to us when we compiled the soundings which form our grids. After we had made our prediction, we obtained the center beam depths from the Hydrosweep survey (S. C. Cande, personal communication, 1993) to compare with our prediction. These data lie in an area of holes in our survey coverage (Figure 1) where our prediction was poorly constrained, so they can put the prediction to a strong test.

Figure 8 (top) shows a profile across the ridge; the profile location is shown in Plate 1. The small crosses are soundings from the *Ewing*, and the curve is drawn showing our prediction at the corresponding points. The Hydrosweep data are very dense, and we have decimated them to only one point per kilometer in Figure 8 for clarity. The bottom panel of Figure 8 shows the *Ewing* soundings and the ETOPO-5 data for comparison. The prediction resolves many details not seen in ETOPO-5, including the correct location of the ridge crest.

We sampled our prediction grid at the *Ewing* data points for 11,748 km of the cruise, and used a linear interpolant to sample both data at 1 km intervals; the two series were then fed to a cross-spectral analysis program (spectrum1d of the Generic Mapping Tools (GMT) system of Wessel and Smith [1991]). The program employs Welch's [1967] method to estimate spectra; we used a window length of 1024 points. We also formed the difference between the *Ewing* data and our prediction and estimated its spectrum by the same method. The results are shown in Figure 9. The power spectral densities (top) are similar at wavelengths longer than 30 km or so, while at shorter wavelengths the prediction has much less power than the *Ewing* data. This is to be expected from the high-cut properties of $W(k)$ (middle). The gain (middle) and

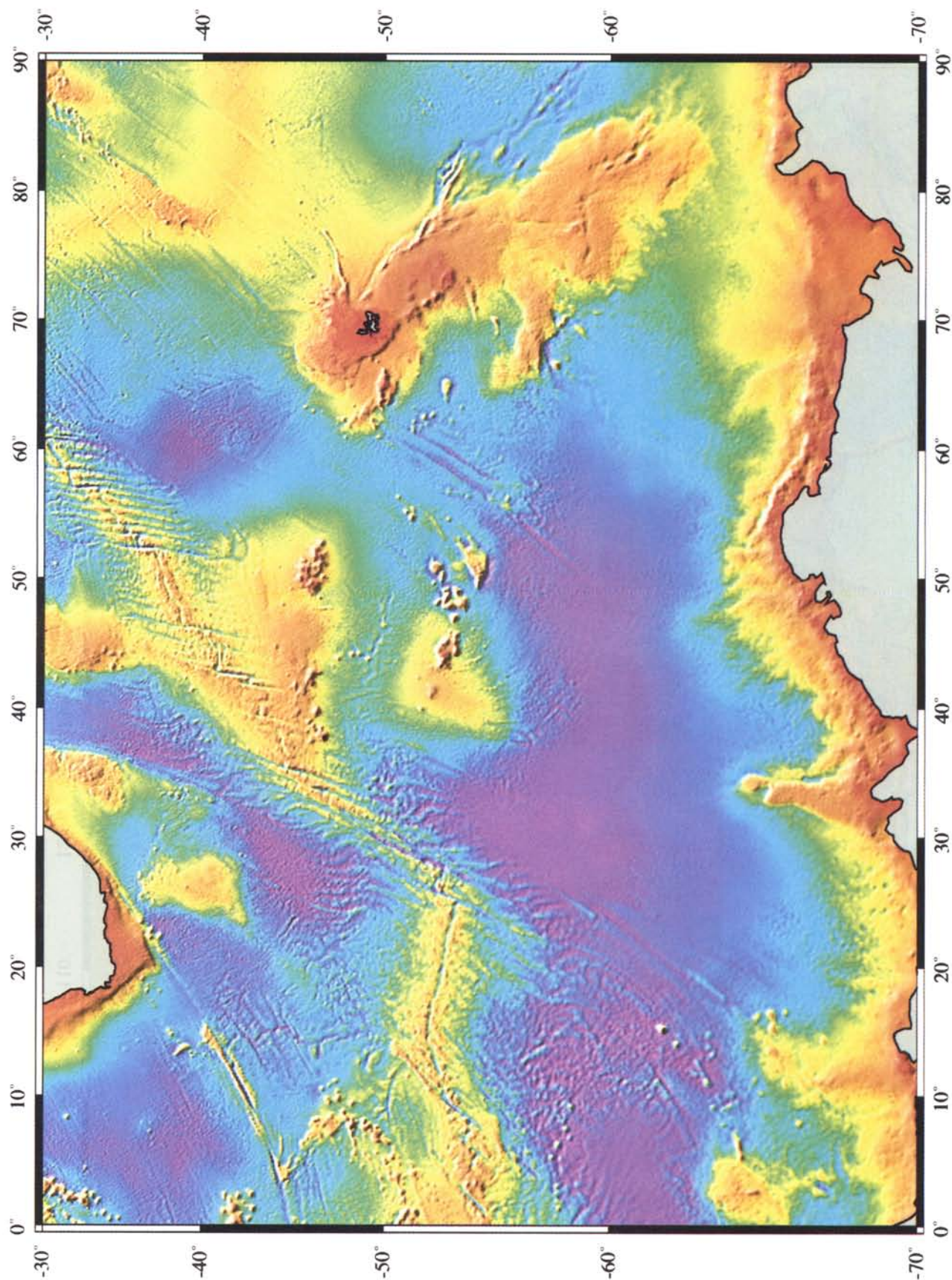


Plate 2. Mercator projection of the bathymetric prediction for the area 0°–90°E.

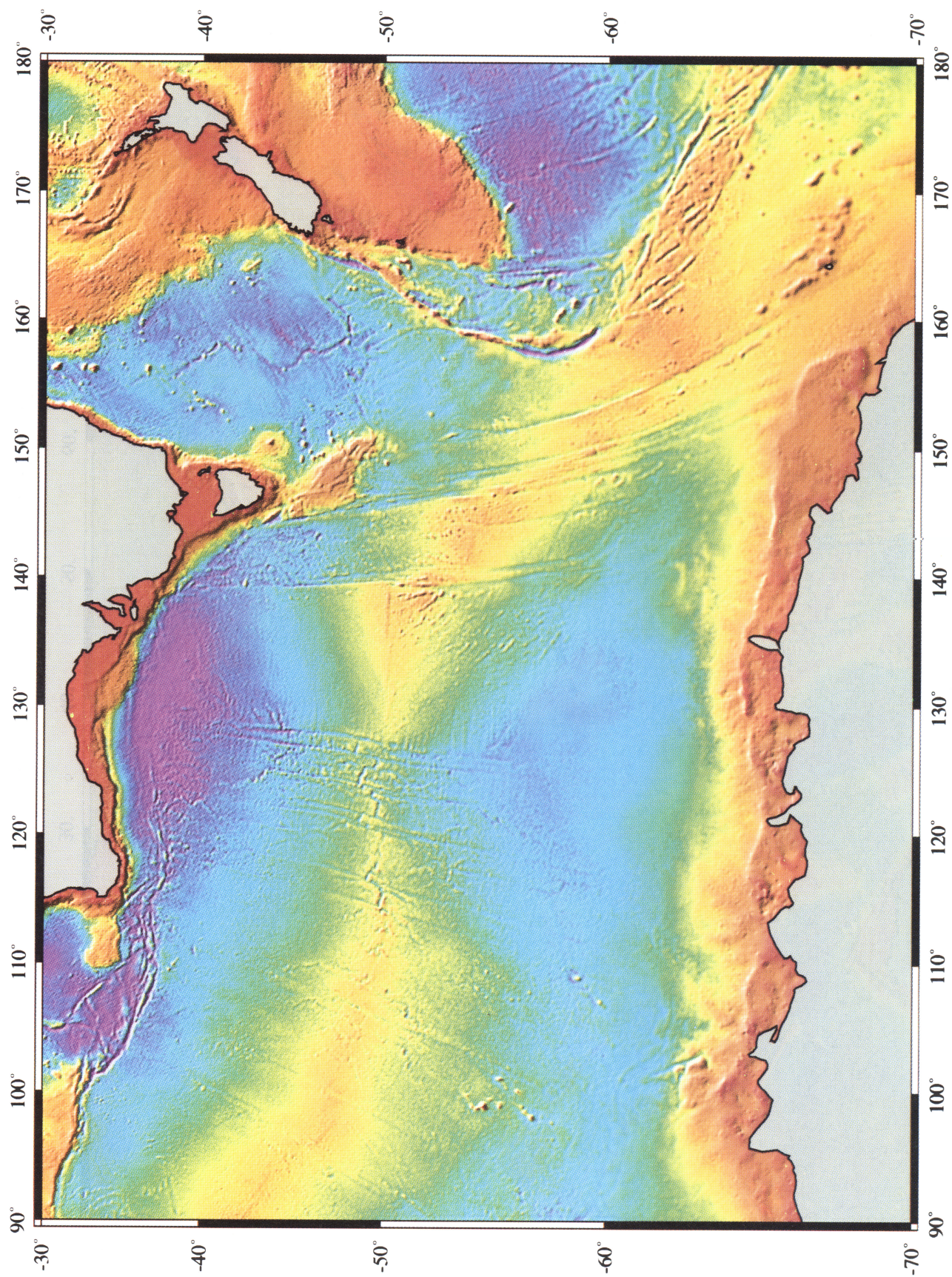


Plate 3. Mercator projection of the bathymetric prediction for the area 90°–180°E.

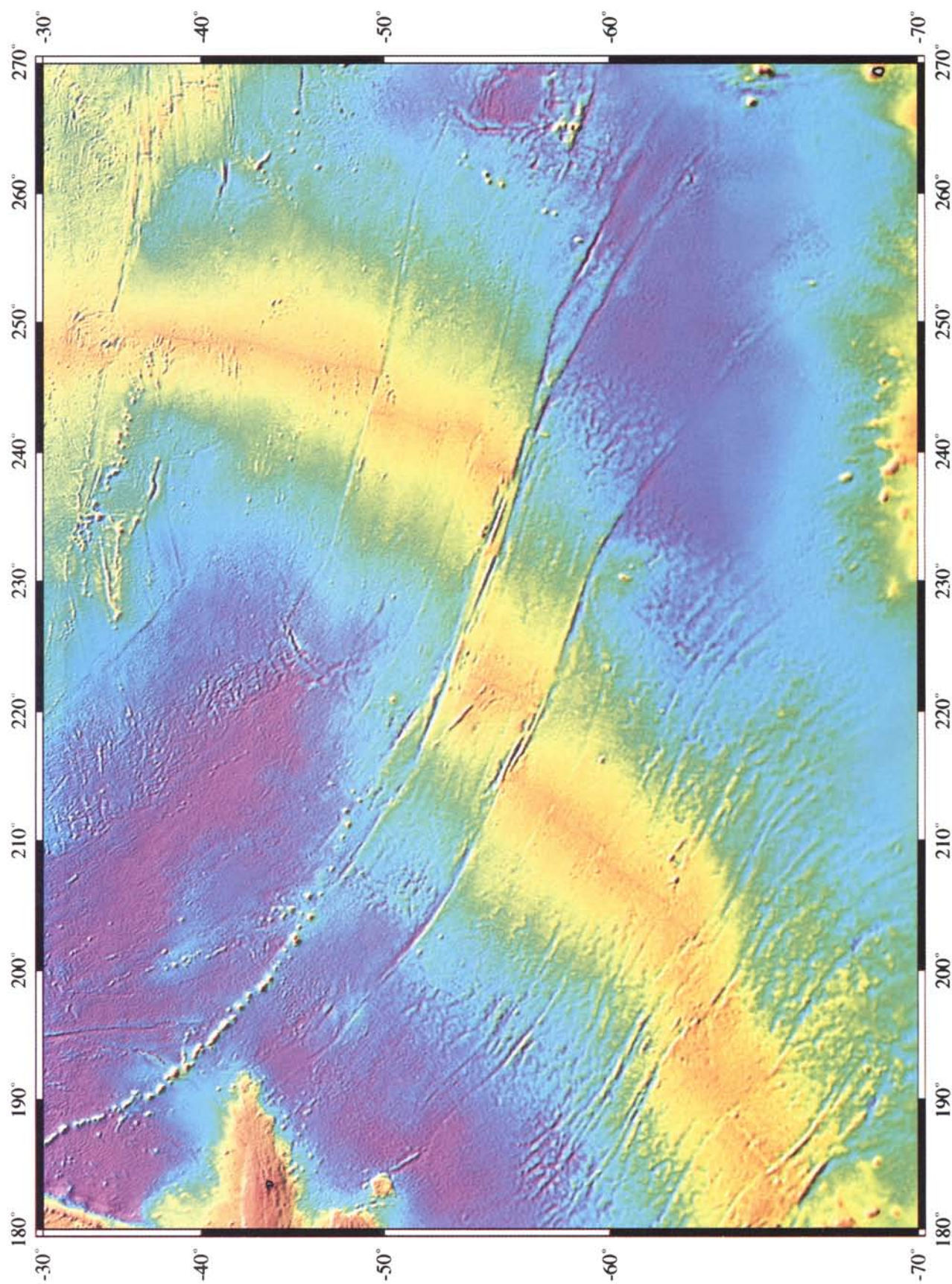


Plate 4. Mercator projection of the bathymetric prediction for the area 180°–270°E.

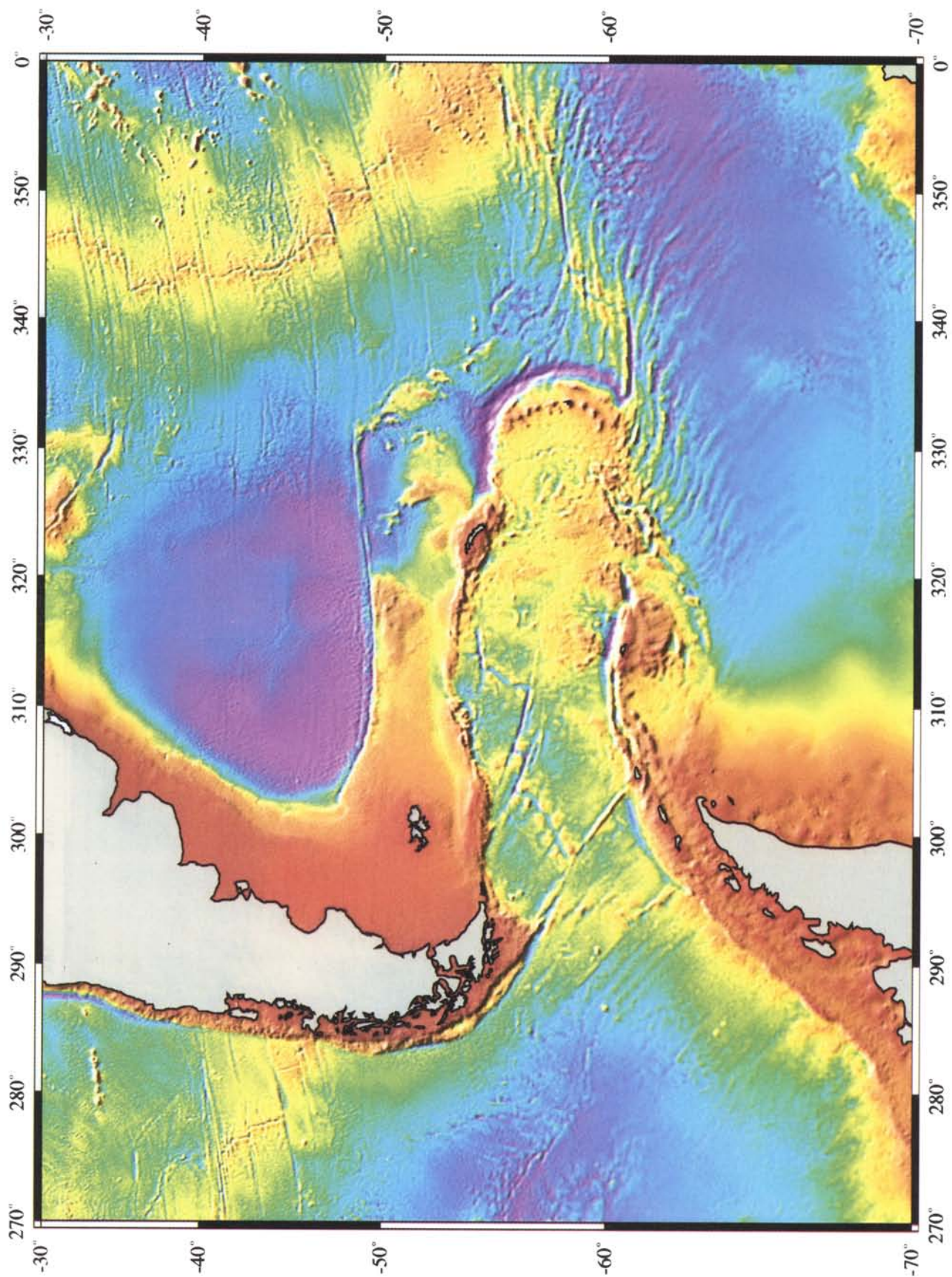


Plate 5. Mercator projection of the bathymetric prediction for the area 270°–360°E.

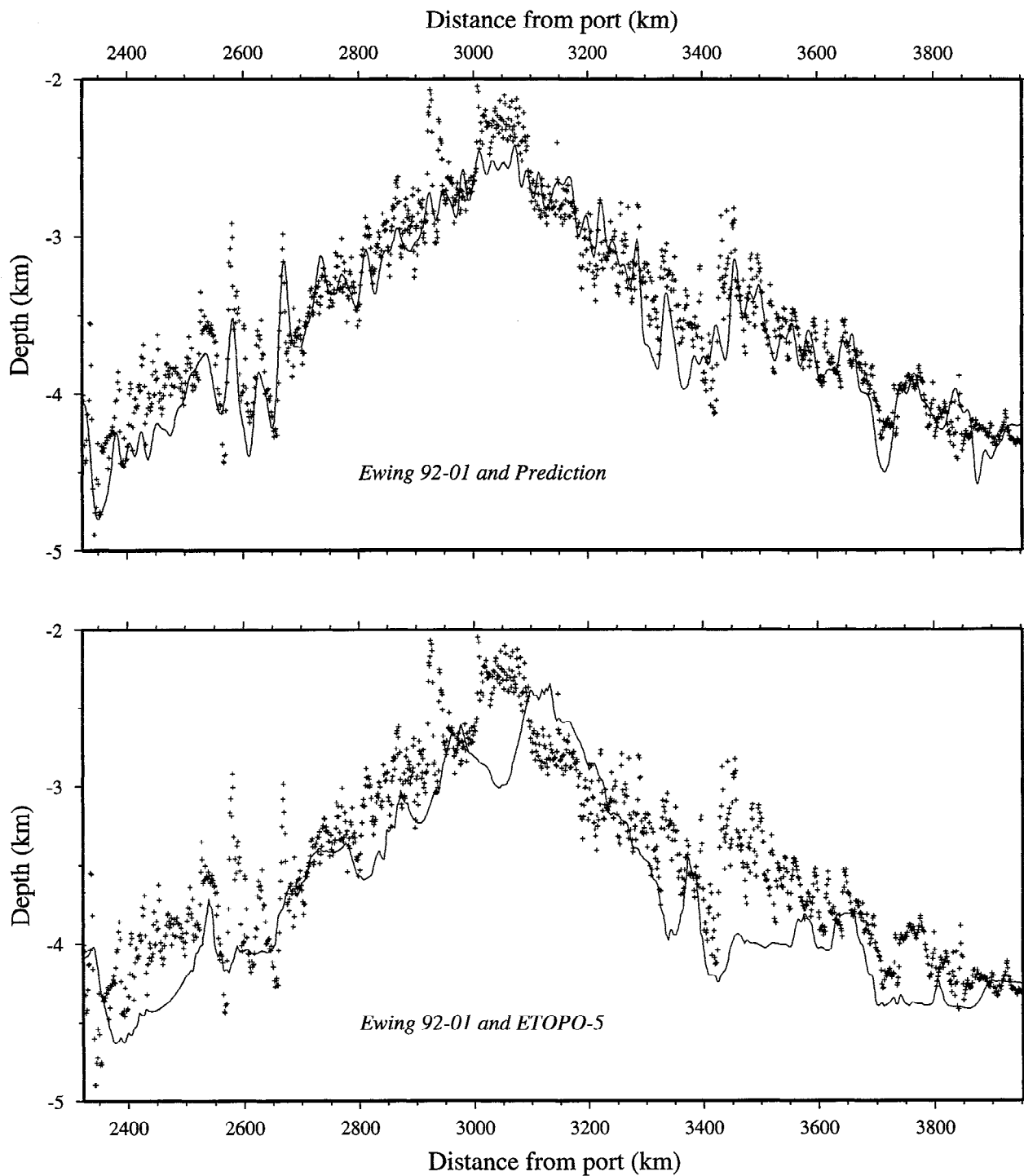


Figure 8. (top) Observed ship soundings (crosses) from R/V *Ewing*, which were not used to constrain the prediction, and the prediction (solid curve). Location of profile is shown in Plate 1. (bottom) Same as top, but solid curve indicates corresponding ETOPO-5 data, not prediction.

coherency (bottom) are calculated assuming that the *Ewing* data are the input and the prediction is the output of a linear system, with noise in the output. The gain and coherency are low at wavelengths shorter than 30 km, again because of the high cut in $W(k)$. An interesting feature of both the gain and coherency plots is that these are slightly higher in the 100-30 km range than they are in the 250-100 km range. The former is within the passband of $W(k)$, where the prediction relies on $S(\mathbf{x})$ and $g(\mathbf{x})$, while the latter is the range where the predic-

tion is based upon $d(\mathbf{x})$, which has been interpolated through the holes in ship coverage. Figure 9 suggests that the interpolated solution is not very good at these wavelengths.

Evaluation and Discussion

We computed the misfit between our prediction and our gridded soundings at all grid points constrained by data. A histogram of the differences is shown in Figure 10 (top). The

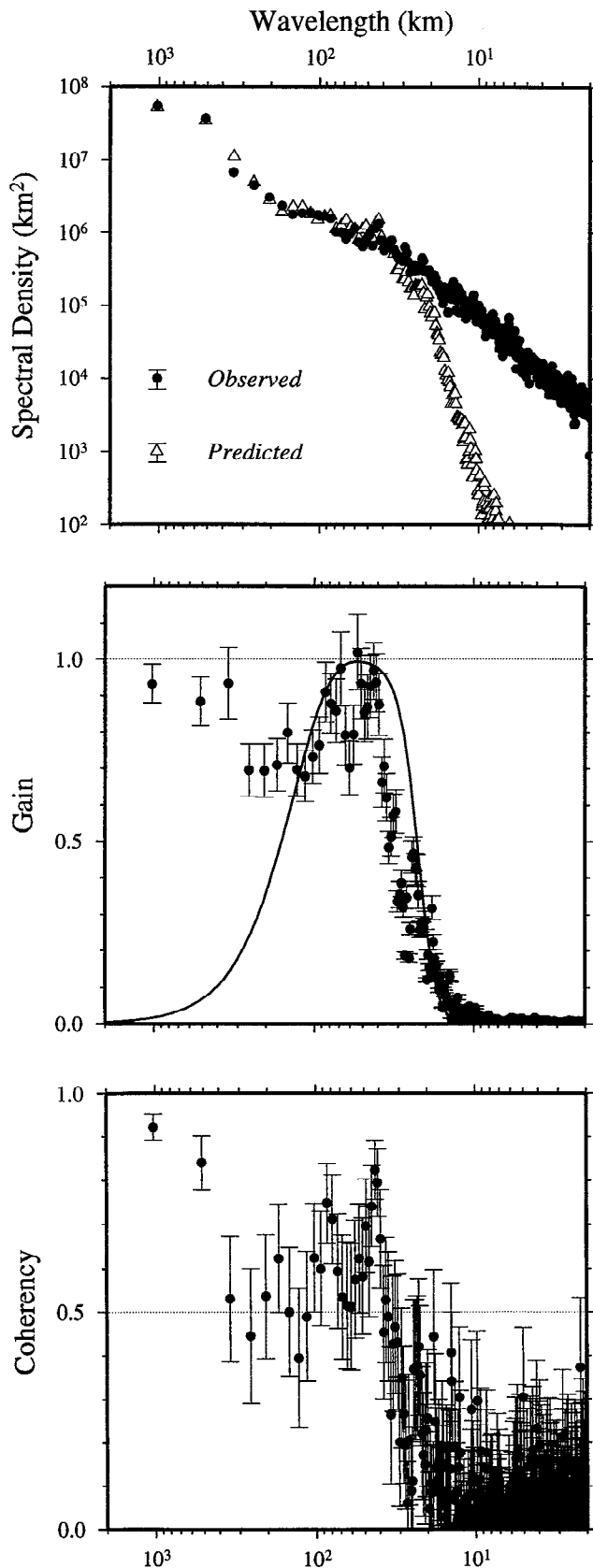


Figure 9. Cross-spectral analysis of *Ewing* data and prediction. (top) Power spectral density. (middle) Gain (coherent amplitude of prediction relative to *Ewing* data), with $W(k)$ for $d=5.5$ km, the average depth of the data. (bottom) Coherency between prediction and *Ewing* data.

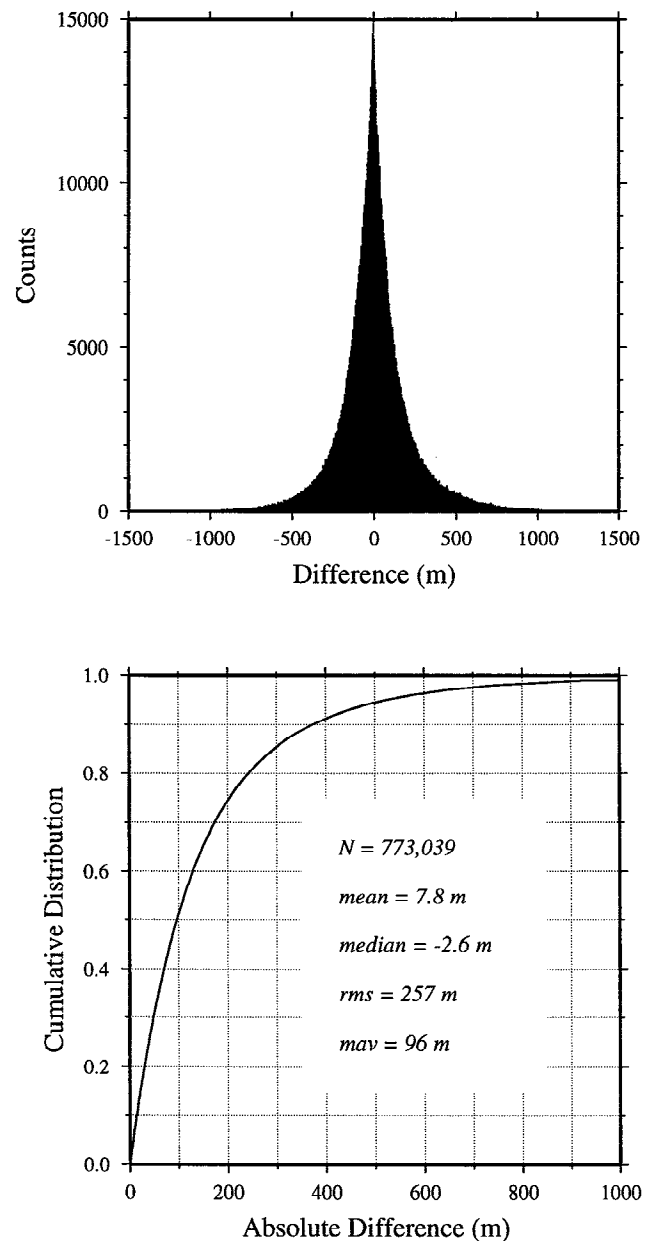


Figure 10. (top) Histogram of differences between prediction and ship soundings shows a distribution more peaked and longer tailed than the normal distribution. (bottom) Cumulative distribution of absolute differences shows that the difference is less than 100 m 50% of the time and less than 240 m 80% of the time.

distribution appears to be symmetric around zero with a sharper peak and longer tails than a normal distribution. The mean difference is 7.8 m and the median difference is -2.6 m. The root-mean-square value (rms) is 257 m and the median absolute value (mav) is 96 m. As explained above, if the distribution were normal, we would expect 1.48 times the median absolute value to equal the root-mean-square value (assuming the distribution to be located at zero); clearly, the rms is much larger due to the long-tailed distribution.

Because of these long tails, the rms and mav do not fully describe the distribution, and so we also computed the cumulative distribution of the absolute value of the differences

(Figure 10, bottom). With this we can see that more than 80% of the differences are less than 257 m, the rms value, whereas a normal distribution would have only 68% at this point. Since the median absolute value is 96 m, 50% of the differences are less than or equal to this value.

A map of the absolute differences is shown in Figure 11 (compare with Figure 7). Shown here are the average absolute differences in 2.5° by 1.25° (135 km) "squares" as used for the Nettleton grid. Squares without data are shown as having an average difference of zero. The very large differences occur in areas of very rugged topography, notably the Scotia Sea, Southwest Indian Ridge, Louisville and Broken Ridges, and Hjort and Chile trenches. There are two reasons why this is expected. The first is that our 2.75 -km grid has a Nyquist wavelength of 5.5 km, while W has a cutoff at 15 – 25 km, depending on water depth, so there can be wavelengths in the observed data grid which we will not predict. In areas of rugged topography, the short wavelengths which are missing from the prediction will be needed to fit the data. The second reason is that in some of these areas the local topography h is not small with respect to d , the regional variation. This is particularly true of features which rise to shallow levels. Under these conditions the approximation that g and h are related by a linear filter is a poor one [Parker, 1973].

The theory given in this paper is based upon the assumption that gravity anomalies (in a limited band, perhaps) are due entirely to seafloor topography. If this is true, then the slope parameter S should be inversely proportional to ρ , the density contrast at the seafloor. Only part of the range of S values we found (Figure 7) can be sensibly inverted for ρ , however. S in the range 13 – 16 m/mGal may be taken to indicate topography composed of basaltic rocks, and slightly higher values of S may be appropriate for continental shelf and slope materials. However, the very small, and perhaps also the very large, values of S indicate conditions that the theory given here is not equipped to handle.

The areas of low (< 10 m/mGal) S and particularly of low correlation and low confidence in rejection of H_0 correspond well with the areas of thick (> 200 m) sediment in the isopach map of Hayes and LaBrecque [1991]. In these areas, the gravity anomalies arise from subsurface structures and not from seafloor topography. At any point where there is some sediment cover over other than flat basement, there may be some contribution to the gravity field from buried structures. Area B (Figure 6b) exhibits a particularly challenging case.

Here the ridge and trough of a major fracture zone meets a thickly sedimented area; sediment has nearly filled the trough, while the ridge is still exposed. This has the effect of clipping the negative h values while making little change in positive h values, leading to the skewed distribution in Figure 6b. Similarly, the positive gravity anomalies are large, while the negative ones are smaller. If the trough is filled completely, the negative gravity anomalies will not vanish, because the sediment-basement density contrast will leave a small negative anomaly. This means that the gravity anomaly distribution must always be less skewed than the topography. The method used here, and indeed any linear filtering method, makes no provision for a S value which depends on the sign of the gravity anomaly; it cannot predict topography with a distribution more skewed than the original gravity anomalies. In the case of area B, one may choose S to fit the ridge and thus predict a too deep trough, choose S to fit the trough and thus underpredict the height of the ridge, or choose an intermediate value and fit both of them badly. One of the reasons we chose slopes based on the Σ method was that it did a better job in situations like area B than other methods we tried.

We are not sure what causes the very large values of S we observe in some areas. These seem to indicate large topographic features associated with unusually low gravity anomalies. One explanation would be that these features are isostatically compensated. We designed the low cut of W (the stopband of W_1) to remove wavelengths affected by compensation, assuming that all areas of the map would have a flexural compensation parameter λ greater than or equal to 135 km. It is possible that some features have a more local compensation (smaller λ). One could try to increase the stopband of W_1 to guard against this, but then the passband of W would become very narrow, leading to other problems. We think our choice of W is a good one. Most of the very large S values occur at the edges of plateaus and continental margins, where there are abrupt and large changes in depth. When these changes are band-pass filtered, the resulting h is probably a significant fraction of d (for a Heaviside step function they would be nearly equal), so that the linear approximation of the gravity-topography relationship does not hold. However, the areas of high S (Figure 7) are not well correlated with the areas of high misfit (Figure 11), so nonlinear effects do not seem to entirely account for the discrepancies.

The horizontal resolution of the prediction is also of interest. We want to know what is the smallest feature that can be resolved and how accurately particular features are located.

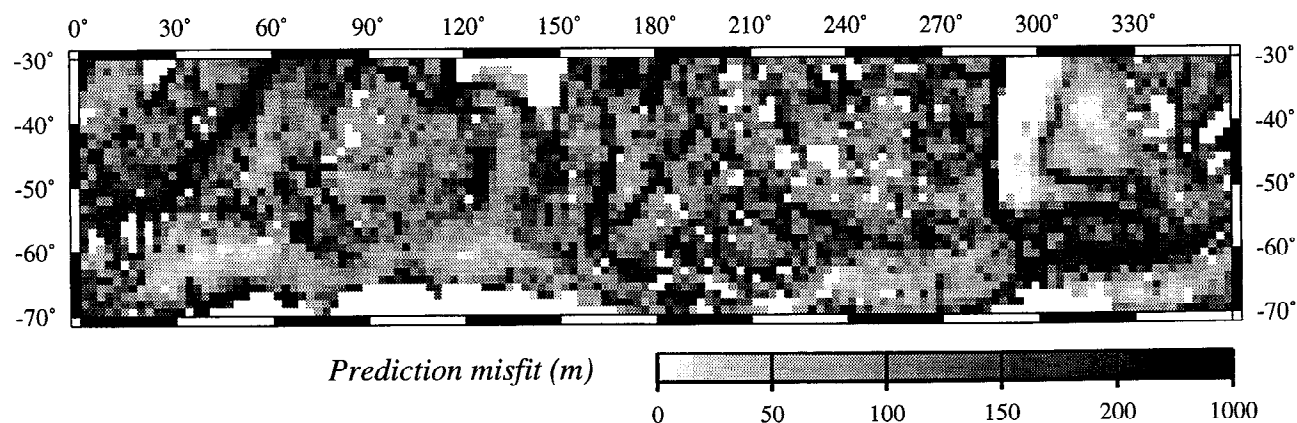


Figure 11. Average absolute difference between prediction and ship soundings in cells same as in Figure 7. Many areas show differences under 50 m. Large differences occur at areas of large variations in topography.

Because the wavelengths shorter than the passband of W are missing from the prediction, this limits the resolution of the prediction. It is clear from Plates 1–5 that the resolution is at least sufficient to distinguish axial highs from axial valleys at mid-ocean ridges. While this paper was in review, P. Lonsdale (personal communication, 1994) made a GPS navigated SeaBeam-2000 survey of the Eltanin and Udintsev Fracture Zones, and found that predicted bathymetric features appeared within the width of the SeaBeam swath. Since the swath width is about 3.4 times the water depth, this experience suggests that the location precision is better than $\pm 1.7d$, or 8 km in deep water. The definitions of resolving power based on length scales in $w(r)$ given above yield more conservative (larger) limits.

As shown by equation (1) and discussed under the inverse Nettleton procedure, our method bases the prediction on gravity data in the passband of W , sometimes (where significant negative correlations exist) in contradiction of the depth sounding data. Smith [1993] has shown that the majority of data may be poorly navigated in much of the southern oceans. In these situations, we believe the gravity data are more likely to be correct than the ship data, and we make no attempt to fit the ship data. Thus our prediction cannot be taken as a summary of, or substitute for, original soundings. Scientists who fit physical models to bathymetric data should be aware of these facts. Since we have produced a prediction which is perfectly correlated with gravity in the passband of W wherever S is nonzero, any attempts to interpret the gravity admittance of our prediction would be circular. Proper uses of our prediction may include (but are not limited to) proposal of new surveys, reconnaissance of tectonic settings, plate reconstructions, ocean current modeling, etc. Our prediction cannot contain very short wavelengths and underestimates topography in rugged areas (Figure 11). We do not guarantee that the actual topography of the ocean floor is as we have predicted.

Conclusions

Flexural isostatic compensation theory suggests that downward continued gravity anomalies should be correlated with seafloor topography in approximately the 15–160 km wavelength band. The theory represents a linear approximation to a nonlinear problem, and the underlying assumption of spatial invariance must be relaxed in order to accommodate regional changes in geology. Stable, high-resolution inversion of gravity data for bathymetric prediction requires careful design of filters to suppress noise in downward continuation.

We find significant correlations between downward continued gravity and topography after these have been band-pass filtered, in areas of rough seafloor topography or where sediment cover is less than 200 m thick. In more heavily sedimented areas, the seafloor appears quite flat, while gravity variations persist; the latter may represent basement topography buried under the sediments. In areas of partial sediment cover, where basement highs are exposed, while lows are filled in, the relationship between gravity and bathymetry cannot be adequately expressed by a linear operation as used here.

We have predicted bathymetry in previously poorly charted waters. Our prediction is validated in an area of the Pacific-Antarctic Ridge by a GPS-navigated Hydrosweep survey. The prediction resolves the location of important tectonic features such as ridge axes better than previously existing gridded data products such as ETOPO-5. The prediction is band-limited and cannot resolve sharp features with their full amplitude; there-

fore the variance of our prediction is less than that of the actual seafloor topography.

We expect that our prediction will be useful in plate reconstructions, analysis of regional trends in topography, and planning of oceanographic cruises. It should not be used in studies of the spectrum of topography data, in particular roughness and topography-gravity admittance studies. It cannot resolve peak amplitudes well, so the predicted depth to the summit of a seamount may not be reliable; safety decisions about hazards to navigation should not be made from it. However, it may be useful in checking the reliability of apparently dubious soundings on old charts.

Appendix: Optimal Downward Continuation of Gravity Data

The exponential growth of downward continuation requires a high-cut filter for stabilization. The choice of cutoff-wavelength is important; too much smoothing will blur the details of seafloor structure, while too little will swamp the prediction with noise. The choice can be formalized using the Wiener theory [Wiener, 1949; Gonzalez and Wintz, 1987] to design a filter which is optimal in the mean-square sense, and the cutoff wavelength can be taken from the results of repeat track coherency studies.

Suppose that we estimate $g(\mathbf{x})$, the gravity field at a depth d , from our gravity observations at sea level, $g_0(\mathbf{x})$, using the downward continuation operator $\exp[2\pi k d]$ and a filter $W_2(k)$:

$$\hat{G}(\mathbf{k}) = G_0(\mathbf{k}) \exp[2\pi k d] W_2(k). \quad (\text{A1})$$

The circumflex on G in (A1) indicates that this is an estimate of the downward continued gravity field. Suppose the true field at depth d is given by

$$G(\mathbf{k}) = S(\mathbf{k}) \exp[2\pi k d], \quad (\text{A2})$$

where $s(\mathbf{x})$ is the "signal" and our observed gravity contains both signal and noise;

$$g_0(\mathbf{x}) = s(\mathbf{x}) + n(\mathbf{x}). \quad (\text{A3})$$

(In this appendix we use S for signal and N for noise; elsewhere S is the slope from the inverse Nettleton procedure.) Now the integrated squared error in our estimate E is

$$E = \iint_{-\infty}^{\infty} [g(\mathbf{x}) - \hat{g}(\mathbf{x})]^2 d\mathbf{x}^2 = \iint_{-\infty}^{\infty} |G(\mathbf{k}) - \hat{G}(\mathbf{k})|^2 d\mathbf{k}^2, \quad (\text{A4})$$

(the second equality in (A4) follows from Rayleigh's theorem [Bracewell, 1978]), and the Wiener filter is that W_2 which minimizes E . When we substitute the first three equations into the fourth, there are signal-noise cross terms SN^* and NS^* (the asterisk indicates a complex conjugate); these are Fourier transforms of the cross covariance between the signal and noise. Assuming that these are uncorrelated, these terms become zero. We assume also that the power spectra of the signal and the noise are isotropic and thus functions of k , not \mathbf{k} , so that

$$E = 2\pi \int_0^{\infty} \exp[4\pi k d] \{ |S(k)|^2 [1 - W_2(k)]^2 + |N(k)|^2 W_2^2(k) \} dk. \quad (\text{A5})$$

A stationary point of E with respect to W_2 is found by setting $\partial E / \partial W_2 = 0$:

$$0 = \frac{\partial E}{\partial W_2} = 4\pi \int_0^\infty \exp[4\pi k d] \{ |N(k)|^2 W_2(k) - |S(k)|^2 [1 - W_2(k)] \} dk. \quad (A6)$$

This point is a minimum for E , which is shown by differentiating again:

$$0 < \frac{\partial^2 E}{\partial W_2^2} = 4\pi \int_0^\infty \exp[4\pi k d] \{ |N(k)|^2 + |S(k)|^2 \} dk. \quad (A7)$$

Now by the calculus of variations, (A6) is satisfied when the integrand is zero, or

$$W_2(k) = [1 + R(k)]^{-1}, \quad (A8)$$

where

$$R(k) = \frac{|N(k)|^2}{|S(k)|^2} \quad (A9)$$

is the amplitude-squared noise-to-signal ratio as a function of wavenumber. Note that W_2 does not depend on the factor $\exp[4\pi k d]$; the Wiener filter is independent of the convolution operator which relates g and g_0 .

Sandwell and McAdoo [1990] have examined the coherency between pairs of Geosat altimeter time series along repeating ground tracks of the Exact Repeat Mission. The coherency in these data can be used to estimate $R(k)$ for the Geosat altimeter. Since the Sandwell and Smith [1992] gravity field is dominated by the Geosat Geodetic Mission data, we expect R for the gridded gravity field to be similar to that obtained by Sandwell and McAdoo [1990]. If we assume that the two samples of altimeter time series have the same signal and noises uncorrelated with the signal and with each other, and the two noises have the same spectrum, then the spectral coherency is

$$\gamma(k) = [1 + R(k)]^{-2} \quad (A10)$$

[Bendat and Piersol, 1986]. The coherency is near 1 when R is small and near 0 when R is large; Sandwell and McAdoo [1990] gave plots of γ and estimates of the wavelength ($1/k$) at which $\gamma = 0.5$. They found that γ is near 1 for long wavelengths and near 0 for short wavelengths, with the transitional wavelength in the range 20–30 km. They showed that the wavelength for $\gamma = 0.5$ varies with the depth to the ocean floor; in deep water ($d = 4$ km) this wavelength is about 30 km, while in shallower water ($d = 2.5$ km) this wavelength is about 20 km. (The values given here are worked out from their results; they give only one example of coherency between two individual time series, and the remaining examples are coherency between pairs of yearly average time series. The wavelengths for $\gamma = 0.5$ given here are appropriate for use in equation (A10).)

Here we create an analytic expression for $R(k)$ which when used in (A10) yields $\gamma(k)$ consistent with the results of Sandwell and McAdoo [1990]. Our expression is inspired by the following guesses about $S(k)$ and $N(k)$: Let the gravity signal arise from application of (5) to a quasi-fractal, random walk topography of the form $H(k)$ proportional to k^{-1} [see Malinverno, 1989, and references therein]; then

$$|S(k)|^2 = A_1 k^{-2} \exp[-4\pi k d], \quad (A11)$$

where A_1 is some constant. Let the noise be white (constant in wavenumber) in the altimeter sea surface height measurement, so that it is proportional to k in the derivative gravity data; then

$$|N(k)|^2 = A_2 k^2, \quad (A12)$$

where A_2 is another constant. Under these assumptions,

$$R(k) = A k^4 \exp[4\pi k d], \quad (A13)$$

where A is an unknown constant. If we choose $A = 80,000$ km⁴, then when we substitute (A13) into (A10) we get $\gamma = 0.5$ when $d = 4$ km and $k = 1/(30$ km), the predicted form for $\gamma(k)$ matches Figure 6b of Sandwell and McAdoo [1990], and the wavelengths at which $\gamma(k) = 0.5$ vary with water depth in the manner described by them. (Small increases in R in areas of large currents were also detected by Sandwell and McAdoo and are not described by (A13).) The Sandwell and Smith [1992] gravity field shows coherency with ship gravity measurements [Smith et al., 1993; Neumann et al., 1993] at shorter wavelengths than the Sandwell and McAdoo study would suggest, and it appears that in shallow water over ridge axes the field has short-wavelength details we want to preserve in our prediction; we therefore chose $A = 9500$ km⁴ rather than 80,000 km⁴.

Note that the derivation leading to (A8) shows that the Wiener filter is independent of the downward continuation term; however, because $R(k)$ depends on depth via (A13), $W_2(k)$ implicitly depends on d .

Acknowledgements. R. L. Parker offered many helpful comments throughout this research. B. T. May raised the question of resolving power and suggested the optical Rayleigh criterion. Many calculations and illustrations were made with the GMT software of Wessel and Smith [1991]. The manuscript was improved with suggestions from A. Goodwillie, K. M. Marks, and D. C. McAdoo and reviews by G. A. Neumann and P. Wessel. This work was supported by the National Science Foundation, Division of Ocean Sciences (OCE 92-17164).

References

- Backus, G., and F. Gilbert, The resolving power of gross Earth data, *Geophys. J. R. Astron. Soc.*, 16, 169–205, 1968.
- Banks, R. J., R. L. Parker, and S. P. Huestis, Isostatic compensation on a continental scale: Local versus regional mechanisms, *Geophys. J. R. Astron. Soc.*, 51, 431–452, 1977.
- Baudry, N., M. Diamant, and Y. Albouy, Precise location of unsurveyed seamounts in the Austral archipelago area using Seasat data, *Geophys. J. R. Astron. Soc.*, 89, 869–888, 1987.
- Bendat, J. S., and A. G. Piersol, *Random Data Analysis and Measurement Procedures*, 2nd ed., 566 pp., John Wiley, New York, 1986.
- Bracewell, R., *The Fourier Transform and Its Applications*, 2nd ed., 444 pp., McGraw-Hill, New York, 1978.
- Brownlee, K. A., *Statistical Theory and Methodology in Science and Engineering*, 2nd ed., 590 pp., John Wiley, New York, 1965.
- Caldwell, J. G., and D. L. Turcotte, Dependence of the thickness of the elastic oceanic lithosphere on age, *J. Geophys. Res.*, 84, 7572–7576, 1979.
- Canadian Hydrographic Service, *General Bathymetric Chart of the Oceans (GEBCO)*, 5th ed., Hydrographic Chart Distribution Office, Ottawa, Canada, 1981.
- Carr, M. H., G. Greeley, K. R. Blasius, J. E. Guest, and J. B. Murray, Some Martian features as viewed from the Viking orbiter, *J. Geophys. Res.*, 82, 3985–4015, 1977.

- Cochran, J. R., An analysis of isostasy in the world's oceans, 2, Mid-ocean ridge crests, *J. Geophys. Res.*, **84**, 4713–4729, 1979.
- Constable, C., and R. Parker, Deconvolution of long-core palaeomagnetic measurements—Spline therapy for the linear problem, *Geophys. J. Int.*, **104**, 453–468, 1991.
- Craig, C. H., and D. T. Sandwell, Global distribution of seamounts from Seasat profiles, *J. Geophys. Res.*, **93**, 10,408–10,420, 1988.
- Dixon, T. H., M. Naraghi, M. K. McNutt, and S. M. Smith, Bathymetric prediction from Seasat altimeter data, *J. Geophys. Res.*, **88**, 1563–1571, 1983.
- Dorman, L. M., and B. T. R. Lewis, Experimental isostasy, 1, Theory of the determination of the Earth's isostatic response to a concentrated load, *J. Geophys. Res.*, **75**, 3357–3365, 1970.
- Ford, P. G., and G. H. Pettengill, Venus topography and kilometer-scale slopes, *J. Geophys. Res.*, **97**, 13,103–13,114, 1992.
- Goodman, J. W., *Introduction to Fourier Optics*, 287 pp., McGraw-Hill, New York, 1968.
- Goodwillie, A. M., and A. B. Watts, An altimetric and bathymetric study of elastic thickness in the central Pacific Ocean, *Earth Planet. Sci. Lett.*, **118**, 311–326, 1993.
- Gonzalez, R. C., and P. Wintz, *Digital Image Processing*, 2nd ed., 503 pp., Addison-Wesley, Reading, Mass, 1987.
- Hayes, D. E., and J. L. LaBrecque, Sediment isopachs: Circum-Antarctic to 30°S, in *Marine Geological and Geophysical Atlas of the Circum-Antarctic to 30°S*, *Antarct. Res. Ser.*, vol. 54, edited by D. E. Hayes, AGU, Washington, D. C., 1991.
- Jung, W.-Y., and P. R. Vogt, Predicting bathymetry from Geosat-ERM and shipborne profiles in the South Atlantic Ocean, *Tectonophysics*, **210**, 235–253, 1992.
- Lewis, B. T. R., and L. M. Dorman, Experimental isostasy, 2, An isostatic model for the U.S.A. derived from gravity and topographic data, *J. Geophys. Res.*, **75**, 3367–3386, 1970.
- Lonsdale, P., Geography and history of the Louisville hotspot chain in the southwest Pacific, *J. Geophys. Res.*, **93**, 3078–3104, 1988.
- Malinverno, A., Testing linear models of sea-floor topography, *Pure Appl. Geophys.*, **131**, 139–155, 1989.
- Mammerickx, J., The Foundation Seamounts: Tectonic setting of a newly discovered seamount chain in the South Pacific, *Earth Planet. Sci. Lett.*, **113**, 293–306, 1992.
- Marks, K. M., and R. V. Sailor, Comparison of GEOS 3 and Seasat altimeter resolution capabilities, *Geophys. Res. Lett.*, **13**, 697–700, 1986.
- Marks, K. M., D. C. McAdoo, and W. H. F. Smith, Mapping the Southwest Indian Ridge with Geosat, *Eos Trans. AGU*, **74**, 81, 86, 1993.
- McKenzie, D. P., and C. Bowin, The relationship between bathymetry and gravity in the Atlantic Ocean, *J. Geophys. Res.*, **81**, 1903–1915, 1976.
- McNutt, M. K., Compensation of oceanic topography: An application of the response function technique to the Surveyor area, *J. Geophys. Res.*, **84**, 7589–7598, 1979.
- National Geophysical Data Center, ETOPO-5 bathymetry/topography data, *Data Announc.* **88-MGG-02**, Natl. Oceanic and Atmos. Admin., U.S. Dep. Commer., Boulder, Colo., 1988.
- National Geophysical Data Center, GEODAS CD-ROM worldwide marine geophysical data, updated 2nd edition, *Data Announc.* **93-MGG-04**, Natl. Oceanic and Atmos. Admin., U.S. Dep. Commer., Boulder, Colo., 1993.
- Nettleton, L. L., Determination of density for reduction of gravimeter observations, *Geophysics*, **4**, 176–183, 1939.
- Neumann, G. A., D. W. Forsyth, and D. Sandwell, Comparison of marine gravity from shipboard and high-density satellite altimetry along the Mid-Atlantic Ridge 30.5°–35.5°S, *Geophys. Res. Lett.*, **20**, 1639–1642, 1993.
- Parker, R. L., The rapid calculation of potential anomalies, *Geophys. J. R. Astron. Soc.*, **31**, 447–455, 1973.
- Parsons B., and J. G. Sclater, An analysis of the variation of ocean floor bathymetry and heat flow with age, *J. Geophys. Res.*, **82**, 803–827, 1977.
- Press, W. H., B. P. Flannery, S. A. Teukolsky, and W. T. Vetterling, *Numerical Recipes*, 818 pp., Cambridge University Press, New York, 1986.
- Rousseeuw, P. J., and A. M. Leroy, *Robust Regression and Outlier Detection*, 329 pp., John Wiley, New York, 1987.
- Sailor, R. V., and M. L. Driscoll, Noise models for satellite altimeter data, *Eos Trans. AGU*, **74**(16), **Spring Meeting suppl.**, 99, 1993.
- Sandwell, D. T., A detailed view of the South Pacific geoid from satellite altimetry, *J. Geophys. Res.*, **89**, 1089–1104, 1984.
- Sandwell, D. T., Antarctic marine gravity field from high-density satellite altimetry, *Geophys. J. Int.*, **109**, 437–448, 1992.
- Sandwell, D. T., and D. C. McAdoo, High-accuracy, high-resolution gravity profiles from 2 years of the Geosat exact repeat mission, *J. Geophys. Res.*, **95**, 3049–3060, 1990.
- Sandwell, D. T., and G. Schubert, Geoid height-age relation from Seasat altimeter profiles across the Mendocino Fracture Zone, *J. Geophys. Res.*, **87**, 3949–3958, 1982.
- Sandwell, D. T., and W. H. F. Smith, Global marine gravity from ERS 1, Geosat, and Seasat reveals new tectonic fabric, *Eos Trans. AGU*, **73**(43), **Fall Meeting suppl.**, 133, 1992.
- Siemens, C. W., On determining the depth of the sea without the use of a sounding line, *Philos. Trans. R. Soc. London*, **166**, 671–692, 1876.
- Smith, W. H. F., On the accuracy of digital bathymetric data, *J. Geophys. Res.*, **98**, 9591–9603, 1993.
- Smith, W. H. F., and D. T. Sandwell, Charting the remote southern oceans with satellite altimetry, *Eos Trans. AGU*, **73**(14), **Spring Meeting suppl.**, 1992.
- Smith, W. H. F., and D. T. Sandwell, *Sea floor topography predicted from satellite altimetry and ship depth measurements*, Rep. MGG-09, World Data Cent. A for Mar. Geol. and Geophys., Natl. Geophys. Data Cent., U.S. Dep. Commer., Boulder, Colo., 1994.
- Smith, W. H. F., and P. Wessel, Gridding with continuous curvature splines in tension, *Geophysics*, **55**, 293–305, 1990.
- Smith, W. H. F., H. Staudigel, A. B. Watts, and M. S. Pringle, The Magellan Seamounts: Early Cretaceous record of the South Pacific isotopic and thermal anomaly, *J. Geophys. Res.*, **94**, 10,501–10,523, 1989.
- Smith, W. H. F., D. T. Sandwell, K. M. Marks, and D. C. McAdoo, On the accuracy of marine gravity fields calculated from satellite altimetry, *Eos Trans. AGU*, **74**(16), **Spring Meeting suppl.**, 99, 1993.
- Van Wyckhouse, R., SYNAPS, *Tech. Rep. TR-233*, U.S. Natl. Oceanogr. Off., Stennis Space Center, Miss., 1973.
- Watts, A. B., An analysis of isostasy in the world's oceans, 1, Hawaiian-Emperor seamount chain, *J. Geophys. Res.*, **83**, 5989–6004, 1978.
- Watts, A. B., On geoid heights derived from Geos 3 altimeter data and flexure of the lithosphere along the Hawaiian-Emperor seamount chain, *J. Geophys. Res.*, **84**, 3817–3826, 1979.
- Watts, A. B., The strength of the Earth's crust, *Mar. Technol. Soc. J.*, **17**, 5–17, 1983.
- Watts, A. B., J. H. Bodine, and N. M. Ribe, Observations of flexure and the geological evolution of the Pacific Ocean basin, *Nature*, **283**, 532–537, 1980.
- Welch, P. D., The use of the fast Fourier transform for the estimation of power spectra: A method based on time averaging over short, modified periodograms, *IEEE Trans. Audio Electroacoust.*, **AU-15**, 70–73, 1967.
- Wessel, P., and W. H. F. Smith, Free software helps map and display data, *Eos Trans. AGU*, **72**, 441, 445–446, 1991.
- White, J. V., R. V. Sailor, A. R. Lazarewicz, and A. R. LeSchack, Detection of seamount signature in Seasat altimeter data using matched filters, *J. Geophys. Res.*, **88**, 1541–1551, 1983.
- Wiener, N., *Extrapolation, Interpolation, and Smoothing of Stationary Time Series With Engineering Applications*, John Wiley, New York, 1949.

D. T. Sandwell, Scripps Institution of Oceanography, Code 0225, La Jolla, CA 92093-0225.

W. H. F. Smith, NOAA, Code N/OES-12, SSMC-4, Station 8423, 1305 East-West Highway, Silver Spring, MD 20910.

(Received December 22, 1993; revised April 11, 1994; accepted April 12, 1994.)